Check for updates

Designer charge-transfer van der Waals heterostructures

T. Huynh,†[a] N. Lee,†[b] Y. Hassan,[c] N. Battulga,[d] K. Muralidharan,[a,e] O. L. A. Monti,[d,f] M. S. Choi (ID) *[c] and B. S. Y. Kim (ID) *[a,d]

Interlayer charge transfer in two-dimensional van der Waals (vdW) heterostructures underpins a wide range of emergent quantum phenomena, ranging from excitonic dynamics and light–matter interactions to various correlated electron states. The ability to manipulate interlayer charge transfer on demand offers a powerful knob to control and functionalize these emergent phenomena. In this review, we discuss the recently emerging strategies for assembling and engineering charge-transfer vdW heterostructures in a programmable fashion. We first discuss various static control knobs for programming interlayer charge transfer, including interfacial band alignment and symmetry breaking interfaces. We next discuss strategies to dynamically modify interlayer charge transfer using light and pressure to perturb charge-transfer heterostructures, with an emphasis on interlayer excitons in transition-metal dichalcogenides. We further highlight new applications that emerge out of these charge-transfer heterostructures, ranging from polaritonic devices to novel transistor architectures and photo- and electro-chemical cells. Finally, we conclude with an outlook and future prospects for a new generation of charge-transfer heterostructures.

1. Introduction

Interlayer charge transfer forms the basis of modern solid-state electronics and optoelectronics. In particular, the redistribution of carriers across material interfaces functionalizes semiconducting materials, for instance by forming depletion regions in p–n junctions and activating transistor operation by doping the semiconducting channel. In conventional bulk semiconductors, such as silicon and GaAs, charge transfer is engineered through ion implantation and substitutional doping, where dopant atoms are introduced directly into the crystal lattice sites. These approaches introduce disorder and scattering sites that fundamentally limit device operation. The technological advancement in the atomic-scale synthesis of semiconducting thin films has enabled a rational design of interlayer charge transfer by manipulating interfacial band alignment in epitaxial semiconductor heterostructures. The modulation doping technique first introduced by Dingle *et al.*

using GaAs/AlGaAs heterostructures represents a hallmark study that leverages this band alignment concept to induce charge transfer from proximal dopant layers into the target interface to achieve a high-mobility two-dimensional electron gas (2DEG).[1] Another representative example is the use of spontaneous polarization effects to induce interfacial charges in polar GaN/AlGaN heterostructures.[2] These charge-transfer heterostructures enabled the realization of tailored band structures with novel electrical and optical properties useful in many modern semiconductor and optoelectronic devices, such as microwave signal processors and avalanche photodiodes.[3,4] More recently, the concept of polarization engineering has surprisingly been shown to induce 2DEG at the interface of two bulk insulating complex oxides $LaAlO_3$ and $SrTiO_3$.[5] In this latter example, the build-up of polarization with the increased thickness of $LaAlO_3$ epitaxially grown on $SrTiO_3$ drives charge transfer to form 2DEG at the $LaAlO_3/SrTiO_3$ interface to compensate for the "polar catastrophe".[6] The extension of charge-transfer heterostructures to oxide thin films and heterostructures has attracted much interest due to their strongly correlated nature of electronic degrees of freedom, including charge, spin, and orbital. This unique characteristic combined with engineered interfacial charge transfer has led to the discovery of a range of emergent phenomena at oxide interfaces, ranging from colossal magnetoresistance to unconventional superconductivity.[7–10]

The recent rise of two-dimensional (2D) materials has fundamentally changed the paradigm of designing interlayer

[a]*Department of Materials Science and Engineering, University of Arizona, Tucson, Arizona 85721, USA. E-mail: briankim@arizona.edu*
[b]*BASIS Oro Valley, Oro Valley, Arizona 85737, USA*
[c]*Department of Materials Science and Engineering, Chungnam National University, Daejeon 34134, Republic of Korea. E-mail: goodcms@cnu.ac.kr*
[d]*Department of Physics, University of Arizona, Tucson, Arizona 85721, USA*
[e]*Lunar and Planetary Laboratory, University of Arizona, Tucson, Arizona 85721, USA*
[f]*Department of Chemistry and Biochemistry, University of Arizona, Tucson, Arizona 85721, USA*
† These authors contributed equally to this work.

charge transfer in solid-state materials systems. The ability to assemble these atomic layers into vdW heterostructures, combined with their exceptional tunability, enables new opportunities to design charge-transfer heterostructures with emergent functionalities without any restrictions to the materials choice.[11] This is in stark contrast to conventional semiconductor and oxide heterostructures described above, in which the materials choice is limited by the specific growth conditions required to stabilize epitaxial thin film heterostructures. However, in earlier years, most studies on 2D materials focused on using a wet transfer to assemble vdW heterostructures, which greatly limited their interfacial quality.[12] Furthermore, early devices fabricated on SiO_2 substrates showed significant presence of disorder in the form of electron–hole charge "puddles" as a result of uncontrolled charge transfer from trapped charged impurities on the SiO_2 surface.[13] The field has rapidly evolved over the past decade towards dry transfer-based assembly of vdW heterostructures in a controlled environment with a precise control over the stacking degrees of freedom.[14–19] The use of vdW substrates and gate metals—such as hexagonal boron nitride (hBN)[20] and graphite,[21,22] respectively—further realized an unprecedented level of interfacial quality amenable to programmable charge-transfer vdW heterostructures.

In this review, we discuss emerging strategies to control interlayer charge transfer in vdW heterostructures in a programmable fashion. We first discuss various strategies to structurally program charge-transfer heterostructures by tailoring band alignment and interfacial symmetry. We next discuss strategies to dynamically control charge-transfer heterostructures, particularly using light- and pressure-induced perturbation of charge transfer with an emphasis on interlayer exciton dynamics in transition-metal dichalcogenides (TMD) heterostructures. We further review emerging applications

based on these charge-transfer heterostructures. This includes the growing class of charge-transfer polaritonic devices, new charge-transfer transistor architectures as well as photo- and electro-chemical cells. Finally, we conclude with a discussion on promising future directions for the discovery of a new generation of charge-transfer heterostructures.

2. Structural control of charge transfer

Electronic band alignment

From a thermodynamic perspective, when distinct materials are brought into contact, the difference in their Fermi levels across the interface and the resultant band alignment drive interfacial charge transfer to equilibrate the system at the interface. This fundamental principle presents an effective approach for doping a target 2D material without directly introducing dopant defects in their lattice sites, which would otherwise lead to detrimental defect-induced scattering of quasiparticles residing in the system. Several powerful approaches have recently been proposed to program charge transfer into the target interface of 2D heterostructures by engineering their interfacial band alignment. One prominent example includes interfacing target 2D materials with a layered high work-function material to artificially create a large misalignment in the Fermi level. For example, Choi et al. assembled WSe_2/graphene heterostructures and oxidized the overlying WSe_2 into a high work-function WO_x using UV-ozone treatment at room temperature (Fig. 1a).[23] The advantage of this approach is that the oxidation process is self-limiting where only the topmost monolayer is oxidized, which subsequently protects underlying layers from getting damaged by UV-ozone treatment.[24,25] Furthermore, the inherently clean WSe_2/graphene interface naturally translates to the WO_x/graphene interface, effectively preventing Fermi level pinning that would otherwise suppress the desired charge transfer.[26] As a result, WO_x/graphene interface induces large hole densities of up to $\sim 3 \times 10^{13}$ cm^{-2} (Fig. 1b). An insertion of WSe_2 or hBN spacers between WO_x and graphene can further reduce the carrier density in graphene to the desired level. This reduction in density follows well a simple electrostatic model that precisely predicts the charge transfer between the constituent layers using the dielectric function of the vdW spacer and work-functions of graphene and WO_x as input parameters.[23,27] Further studies demonstrated the encapsulation of graphene with WO_x to induce charge transfer from both the top and bottom surfaces of graphene, which resulted in an enhancement of the doping density in graphene up to $\sim 5 \times 10^{13}$ cm^{-2}.[27,28] In a related study, other oxidized TMDs—such as MoO_x (by oxidizing MoS_2)[29] or ZrO_x (by oxidizing $ZrSe_2$)[27]—were employed to induce hole and electron transfer into graphene, respectively (Fig. 1c and d). The work-function of the latter ZrO_x (~ 3.4 eV) is significantly smaller than that of graphene, uniquely inducing electron transfer into graphene.[27]

Prof. B. S. Y. Kim received his B. S. degree in Electrical Engineering from Northwestern University. He went onto receive his M.S. and Ph.D. degrees in Electrical Engineering from Stanford University where he worked on complex oxide heterostructures and devices. He was then a post-doctoral researcher at Columbia University working on 2D materials and nano-optical imaging. Currently, he is an assistant professor at the Departments of Materials Science and Engineering and Physics at the University of Arizona. His research interest focuses on designing low-dimensional quantum materials and charge-transfer heterostructures for a new generation of electronic, photonic and quantum technologies.
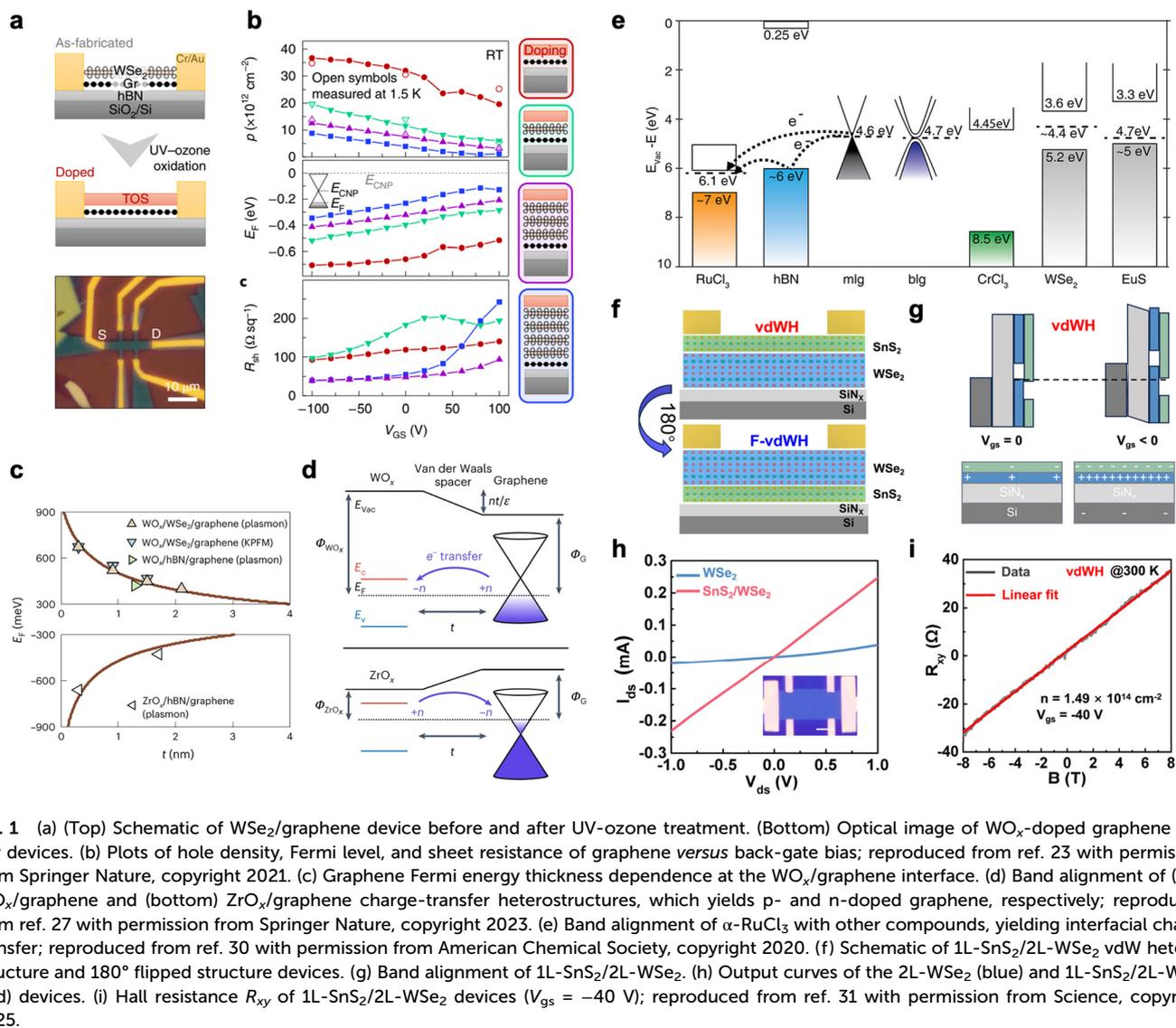
B. S. Y. Kim

Fig. 1 (a) (Top) Schematic of WSe_2/graphene device before and after UV-ozone treatment. (Bottom) Optical image of WO_x-doped graphene Hall bar devices. (b) Plots of hole density, Fermi level, and sheet resistance of graphene *versus* back-gate bias; reproduced from ref. 23 with permission from Springer Nature, copyright 2021. (c) Graphene Fermi energy thickness dependence at the WO_x/graphene interface. (d) Band alignment of (top) WO_x/graphene and (bottom) ZrO_x/graphene charge-transfer heterostructures, which yields p- and n-doped graphene, respectively; reproduced from ref. 27 with permission from Springer Nature, copyright 2023. (e) Band alignment of α-$RuCl_3$ with other compounds, yielding interfacial charge transfer; reproduced from ref. 30 with permission from American Chemical Society, copyright 2020. (f) Schematic of 1L-SnS_2/2L-WSe_2 vdW heterostructure and 180° flipped structure devices. (g) Band alignment of 1L-SnS_2/2L-WSe_2. (h) Output curves of the 2L-WSe_2 (blue) and 1L-SnS_2/2L-WSe_2 (red) devices. (i) Hall resistance R_{xy} of 1L-SnS_2/2L-WSe_2 devices ($V_{gs} = -40$ V); reproduced from ref. 31 with permission from Science, copyright 2025.

The same approach of inducing charge transfer by designing the relative band alignment has also recently been adopted at the heterointerface between two 2D materials. For example, Wang *et al.* employed layered α-$RuCl_3$ as a high work-function charge transfer layer by interfacing it with graphene to heavily hole dope graphene up to ~3×10^{13} cm^{-2} (Fig. 1e).[30] Moore *et al.* showed that multilayer graphene encapsulated within two α-$RuCl_3$ layers can induce carrier densities in multilayer graphene as high as ~8×10^{13} cm^{-2}.[32] Lee *et al.* further demonstrated a remote modulation doping strategy for semiconducting TMDs.[33] Interestingly, this study showed that depositing an n-type molecular dopant triphenylphosphine (PPh_3) on WSe_2 enables charge transfer into a remote, underlying MoS_2 layer that is physically separated by an hBN spacer. Here, the specific band alignment between WSe_2 and MoS_2 layers promotes the charges activated from the PPh_3 layer on the surface to be transferred vertically across WSe_2, deep into the MoS_2 layer. A similar effect has also been observed in

organic/inorganic vdW heterostructures consisting of K adatoms, graphene, and a Pb monolayer. In this latter structure, nearly 44% of the electrons donated by the K adatoms bypass the directly adjacent graphene layer to dope the buried Pb monolayer due to the specific band alignment of the heterostructure.[34] In a related study, Zhao *et al.* realized a "hyper-doping" effect in SnS_2/WSe_2 heterostructures,[31] reaching a remarkably high hole density of ~1.5×10^{14} cm^{-2} in WSe_2 (Fig. 1f–i). In the absence of an external electrostatic field, SnS_2/WSe_2 heterostructures exhibit a type III broken band alignment, driving electron transfer from WSe_2 valence band to SnS_2 conduction band. This configuration results in the hole doping of WSe_2 to a nominal carrier density of ~1×10^{13} cm^{-2}. Strikingly, when a back-gate voltage is applied across SiO_2 gate dielectric in SnS_2/WSe_2/SiO_2/Si structures, the heavily hole-doped WSe_2 partially screens the electrostatic field. This partial screening induces an unequal energy level shift between WSe_2 and SnS_2 bands, thereby dynamically

increasing the broken-band offset at the interface and drastically enhancing the hole transfer from SnS_2 to WSe_2 up to ~1.5 × 10^{14} cm^{-2}.

Twist angle and interfacial symmetry

The rate and direction of interlayer charge transfer across vdW heterostructures depend not only on the intrinsic band alignments but also critically on how individual layers are stacked and oriented with respect to each other. For example, twisting two vdW layers can significantly alter their interfacial orbital overlap, built-in electric fields, and electric field screening, leading to drastic modifications in the interlayer charge transfer dynamics. The resonant tunnelling phenomena of charge carriers across such a twisted vdW heterostructure is of particular interest as it enables anomalous current–voltage characteristics across the interface, including negative differential resistance (NDR). Mishchenko et al. demonstrated that charge transfer across two twisted graphene monolayers (small rotation angles of <2°) separated by an atomically thin hBN leads to a resonant tunneling effect with NDR behavior (Fig. 2a and b).[35] The resonant condition exists in a narrow bias window that conserves the in-plane energy and momentum of the tunneling electrons. This effect is maximized when the momentum difference between two Dirac cones of individual graphene layers is electrostatically compensated by tuning the energy difference of the same Dirac cones via biasing. In these devices, the peak-to-valley current ratio (PVCR), which quantifies the magnitude of NDR, reaches ~2 at room temperature. Srivastava et al. dramatically enhanced PVCR to ~9 based on twisted black phosphorus (BP) homostructures, particularly without a tunnel barrier that would otherwise suppress PVCR as well as the overall current levels (Fig. 2c and d).[36] Here, the discrete levels of quantum-well states (QWS) are created in non-degenerate BP layer (<14 atomic layers thick) by encapsulating it with thicker degenerate BP layers on the top and bottom, twisted with respect to each other. Resonant tunneling is achieved when the energy and momentum of electrons injected from thicker BP layers matches those of bound QWSs due to energy and momentum conservation. Recently, Zhang et al. identified that in graphene-based NDR devices, edge doping near the perimeter of graphene can locally shift the energy position of Dirac cone and extrinsically reduce the PVCR values (Fig. 2e–g).[37] This edge doping effect can be suppressed by rationally designing the etching geometry of graphene layers to reduce the area-to-perimeter ratio. As a result, PVCR of ~15 was achieved at room temperature.
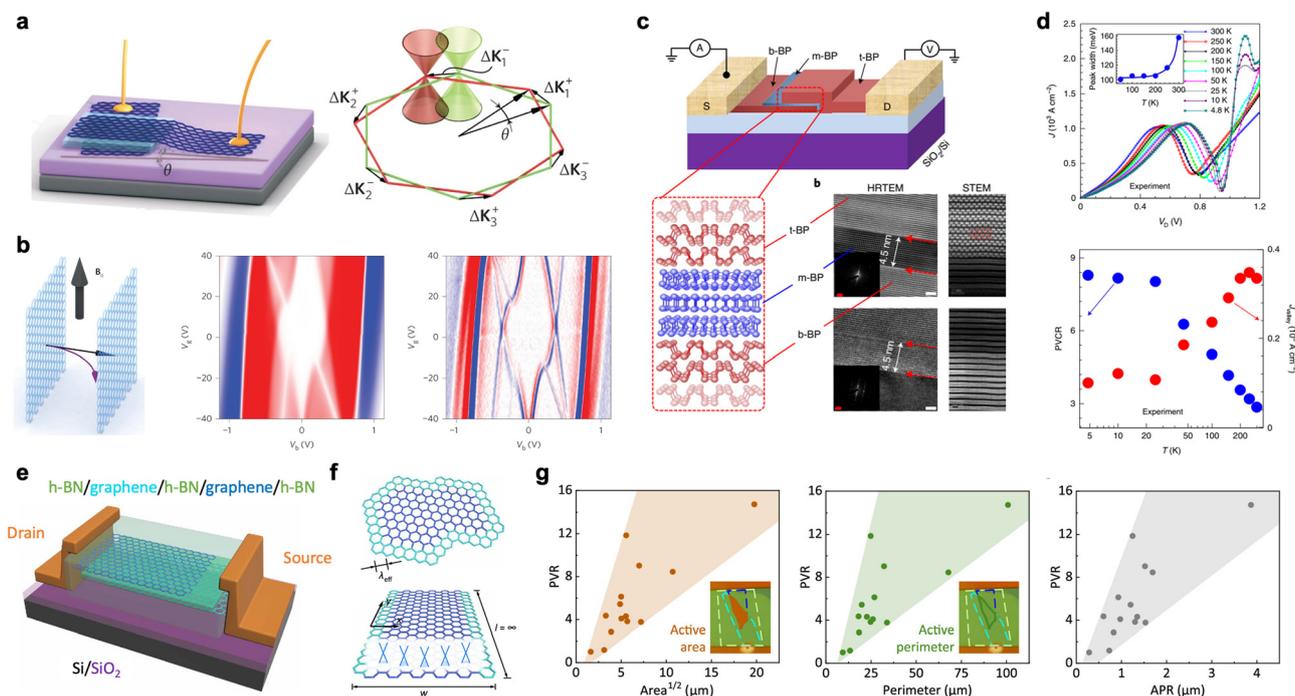

Fig. 2 (a) Schematic of (left) exaggerated angle θ between two graphene layers and (right) the associated momentum shift between two Dirac points. (b) (Left) Trajectories of charged quasiparticles tunneling from top to bottom graphene layers. Experimental data for (middle) dI/dV maps with in-plane B field and (right) differential dI/dV maps with and without the in-plane B field; reproduced from ref. 35 with permission from Springer Nature, copyright 2014. (c) Device structure of trilayer orthogonal BP homojunctions. (d) (Top) Temperature-dependent current−voltage characteristics, and (bottom) temperature-dependent evolution of the peak-to-valley current ratio (PVCR) and valley current density (J_{valley}) of a trilayer orthogonal homojunction device with m-BP layer number of ~7 L; reproduced from ref. 36 with permission from Springer Nature, copyright 2021. Schematic of (e) graphene resonant tunneling diodes (GRTD). (f) Edge doping in graphene flake of an arbitrary shape (top) and graphene ribbon (bottom). (g) Peak-to-valley ratio (PVRs) of 14 devices as a function of (left) area, (middle) perimeter, and (right) area-to-perimeter ratio (APR); reproduced from ref. 37 with permission from American Chemical Society, copyright 2023.

Another interesting direction to control charge transfer is by breaking global and local interfacial symmetry, which can lead to the spontaneous redistribution of charge carriers within the materials system. A representative example is the spontaneous formation of interlayer ferroelectric dipoles in marginally twisted vdW heterostructures. For example, Zheng *et al.* reported the emergence of ferroelectricity in bilayer graphene encapsulated and aligned parallel to the top and bottom hBN layers (Fig. 3a).[38] This is surprising given that conventional forms of ferroelectricity arise in polar materials from a spatial separation of cations and anions from their equilibrium position. Here, the observed ferroelectricity in nonpolar bilayer graphene is ascribed to a combination of moiré- and gate-induced layer asymmetry in the band structures and electron interactions, which drive charge transfer between the top and bottom layers of bilayer graphene. In a related study, Niu *et al.* showed that interfacial ferroelectricity in marginally twisted bilayer graphene/hBN systems exists even when the

Fermi level lies deep inside the dispersive bands beyond the low-lying moiré bands.[39] This latter observation calls for further experimental studies to elucidate the microscopic origin of the ferroelectricity. After this initial discovery, the scope of 2D materials displaying interfacial ferroelectricity has rapidly expanded to other non-polar candidates, including marginally-twisted hBN[40–43] and TMDs[44–48] (Fig. 3b and c). In these latter systems, interfacial ferroelectricity arises from the broken inversion symmetry at the moiré interface combined with lattice-scale interlayer sliding. Recent studies further revealed exciting utility of these systems, including ultrafast nanoscale switching with extremely high endurance exceeding 10^{11} cycles of polarization switching[49] as well as superlubricity-induced polytype switching.[50]

On another front, Janus TMDs represent an exciting alternative platform that exhibits intrinsic interlayer electrical dipole due to their mirror symmetry-broken crystal structure that arises from a distinct top and bottom chalcogenide atomic layer. A recent
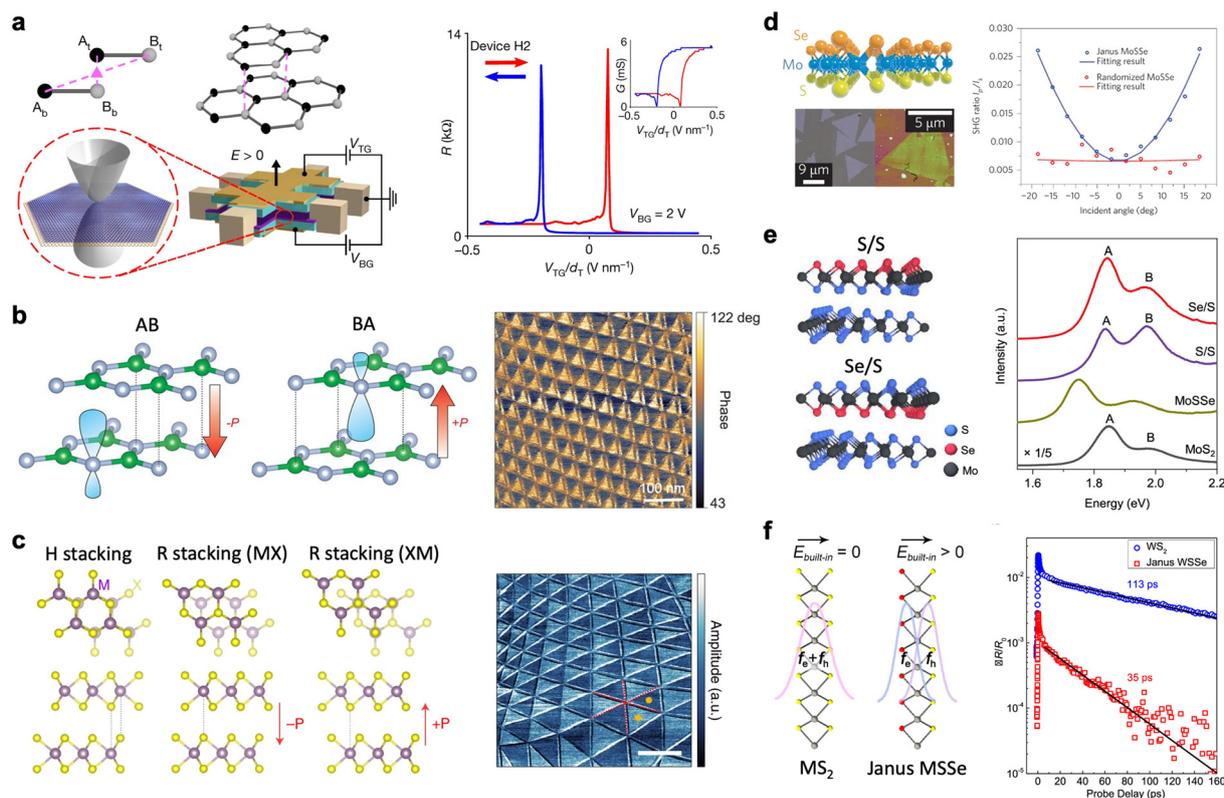

Fig. 3 (a) (Left) Schematic of atomic structure of Bernal-stacked bilayer graphene and device structures with top and bottom gates. (Right) Gate-tuned resistance of the hysteretic devices; reproduced from ref. 38 with permission from Springer Nature, copyright 2020. (b) (Left) Schematic of different atomic arrangement for AB- and BA-stacked hBN homobilayer with induced ferroelectricity. (Right) Vertical PFM phase image of twist bilayer hBN; reproduced from ref. 40 with permission from Science, copyright 2021. (c) (Left) Atomic structure of H-stacked, R-stacked (MX and XM) bilayer TMD. (Right) Amplitude image of vertical PFM on MoSe$_2$; reproduced from ref. 44 with permission from Springer Nature, copyright 2022. (d) (Left) Atomic structure, optical microscopy, and atomic force microscopy images of Janus MoSSe. (Right) SHG intensity as a function of incident angle; reproduced from ref. 51 with permission from Springer Nature, copyright 2017. (e) (Left) Atomic structure of heterobilayers with S/S and Se/S interface. (Right) PL spectra of MoS$_2$ monolayer, MoSSe monolayer, and twisted heterobilayers with S/S and Se/S interface; reproduced from ref. 52 with permission from American Chemical Society, copyright 2021. (f) (Left) Side view of MS$_2$ and Janus MSSe. (Right) Pump–probe differential reflectance signal *versus* the probe photon energy for Janus WS$_2$ and WSSe; reproduced from ref. 53 with permission from American Chemical Society, copyright 2021.

success in chemically synthesizing Janus TMDs[51,54,55] has motivated a significant interest in manipulating charge transfer by leveraging the sizable out-of-plane dipole that arises from their intrinsic structural asymmetry (Fig. 3d). For example, the charge transfer across the Janus/regular TMD interface is highly direction dependent. In SWSe/WS$_2$ and SWSe/WSe$_2$ heterostructures, the photoexcited charge transfer along the built-in field direction is ultrafast and efficient, whereas that in the opposite direction is highly inefficient and slow.[56] Zhang *et al.* further corroborates these phenomena by observing that the charge transfer-induced quenching of photoluminescence is enhanced in MoSSe/MoS$_2$ heterostructures when the built-in field is parallel to the charge transfer direction (Fig. 3e).[52] The built-in field also directly controls the intrinsic dynamics of excitons within Janus TMDs. For example, Zheng *et al.* elucidated that exciton formation in MoSSe and WSSe is faster than their regular TMD counterparts due to enhanced electron–phonon interaction driven by the built-in field (Fig. 3f).[53] This enhanced interaction in turn facilitates optical phonon-mediated exciton formation. Furthermore, a drastically longer exciton radiative recombination lifetime has been observed in Janus structures compared to the regular TMDs due to a more efficient spatial separation of electron and hole wave functions *via* the built-in dipole.

3. Dynamic control of charge transfer

Light-induced charge transfer

Photoexcitation of vdW heterostructures is amenable to the separation of excited electron–hole pairs into the neighboring

atomic layers *via* interlayer charge transfer. TMD heterobilayers with type II band alignment particularly drive these photo-excited electron–hole pairs into neighboring layers to form an interlayer exciton—a Coulomb-bound electron–hole pair, where each charge resides in neighboring layers. Interlayer excitons were first observed in photoexcited MoS$_2$/WS$_2$ heterostructures, in which the interlayer charge transfer takes place at an ultrafast timescale of ~50 fs after photoexcitation (Fig. 4a).[57] Remarkably, the physical separation of electron–hole pair in respective layers render these interlayer excitons extremely long-lived with their lifetime approaching ~1.8 ns. Since this initial discovery, interlayer excitons were observed in a wider range of TMD heterostructures with type II band alignment.[58–66] Notably, ultrafast interlayer charge transfer (typically on the order of sub 100 fs scale) is universally observed in most of these TMD heterostructures, which is unusual considering the momentum mismatch and weak interlayer coupling across the vdW interface. However, the physical mechanism of this ultrafast charge transfer and interlayer exciton formation has remained relatively underexplored.

Recent studies suggest that phonon scattering plays a dominant role in mediating the interlayer charge transfer and interlayer exciton formation in these systems. For example, Policht *et al.* interestingly discovered that interlayer exciton formation in MoSe$_2$/WSe$_2$ heterostructures occurs at a significantly later time (~1 ps) than the rapid charge transfer timescale (~100 fs).[69] This relative delay in the exciton formation is attributed to the combination of the following two processes. One is the energy and momentum relaxation of hot intra-exciton population, and the other is the phonon-mediated cascade process of higher energy excitons decaying into their ground state. In a
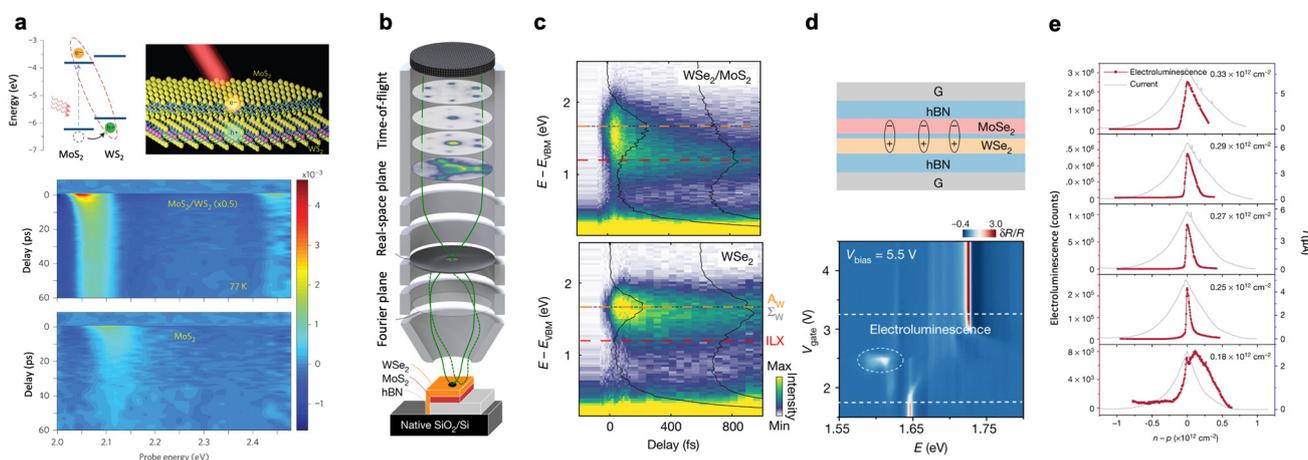

Fig. 4 (a) (Top) Schematic diagram of interlayer exciton formation in MoS$_2$/WS$_2$ heterostructure with type II band alignment. Transient absorption spectra *versus* probe energy at 77 K in (middle) MoS$_2$/WS$_2$ heterostructure and (bottom) MoS$_2$ monolayer upon MoS$_2$ A-exciton excitation; reproduced from ref. 57 with permission from Springer Nature, copyright 2014. (b) Schematic of femtosecond momentum microscopy. (c) Pump–probe delay dependent evolution of the momentum-integrated energy-distribution curves for (top) WSe$_2$/MoS$_2$ heterostructures and (bottom) isolated WSe$_2$; reproduced from ref. 67 with permission from Springer Nature, copyright 2022. (d) Schematic of MoSe$_2$/WSe$_2$ heterobilayer devices with electron–hole double-layer structures. (Top) Differential reflection, $\delta R/R$, *versus* photon energy E and gate voltage V_{gate}. Electroluminescence from the tunnel junction is visible in the circled bright spot. (e) (Left axis) Electroluminescence intensity and (right axis) tunnelling current *versus* electron–hole density imbalance for variable total densities. A threshold behavior with a cusp-shaped peak emerges, indicative of the formation of exciton condensation; reproduced from ref. 68 with permission from Springer Nature, copyright 2019.

related study, Wagner *et al.* also observed the aspect of spin-valley polarization in interlayer excitons mediated by phonon scattering in the same photoexcited $MoSe_2$/WSe_2 hetero-structures.[70] The experimental findings show that the spin-valley polarization of initial photoexcited intralayer excitons is conserved during the charge transfer and the interlayer exciton formation processes, particularly at low temperatures. But the degree of spin-valley polarization is significantly decreased at higher temperatures due to phonon scattering. Furthermore, Sood *et al.* employed femtosecond electron diffraction to observe the mechanism of photoexcited interlayer exciton formation in WSe_2/WS_2 heterobilayers.[71] Careful studies revealed that the charge transfer occurring at femtosecond timescale is accompanied by bidirectional phonon emission, after which both WSe_2 and WS_2 layers are simultaneous heated on a pico-second timescale. This process is ascribed to the interlayer hybridized electronic states mediating concurrent phonon emission in each WSe_2 and WS_2 layer during the interfacial charge transfer. In a related study, Schmitt *et al.* observed that interlayer exciton formation in WSe_2/MoS_2 heterobilayers is prompted by exciton–phonon scattering at femtosecond time-scale, followed by subsequent charge transfer mediated by interlayer-hybridized valence band (Fig. 4b and c).[67]

Beyond single-exciton dynamics, another emerging frontier lies in leveraging many–body exciton–exciton interactions to engineer strongly correlated phases based on TMD heterobilayers. One important prerequisite for realizing strong exciton–exciton interaction is long exciton lifetime to ensure a long exciton interaction time. In this respect, the insertion of atomically thin hBN spacer layer at the interface of TMD heterobilayers has proven effective in enhancing the interlayer exciton lifetime. Such a structure has been employed to realize new excitonic phases in TMD heterostructures, including excitonic insulators[72,73] and Bose–Einstein condensates[68] (Fig. 4d and e). Another strategy to enhance exciton–exciton interaction is by engineering the dielectric environment of TMD heterobilayers. For example, free-standing WSe_2/WS_2 heterobilayers with minimized dielectric screening induce the transition from repulsive to attractive dipolar interaction among interlayer excitons as a result of exchange–correlation effects.[74] This strongly enhanced many–body interaction of interlayer excitons enabled the observation of previously elusive interlayer biexcitons. Finally, moiré-trapped excitons represent another robust platform that enables the fine-tuning of exciton–exciton coupling strengths *in situ*. Recent studies revealed that at small interlayer twist angles, interlayer excitons are laterally localized within the respective moiré superlattice potential sites.[75–78] These moiré-trapped excitons may serve as a robust platform for realizing tunable exciton–exciton interactions by precisely controlling the interlayer twist angle.[79] Using this approach, one can effectively modify the moiré potential landscape as well as the exciton–exciton distance, thereby continuously tuning the exciton–exciton coupling strengths. This platform provides a viable pathway towards exotic many–body excitonic phenomena, such as Dicke superradiant phase transition that emerges from strongly coupled arrays of quantum emitters.

Pressure-induced strain engineering

The use of pressure to control strain configuration represents a powerful and clean method to tune interlayer charge transfer in vdW heterostructures by directly altering interlayer spacing and lattice structures.[80] For example, hydrostatic pressure reduces the interlayer gap in vdW heterostructures and promotes interlayer coupling, making it an efficient approach for tuning charge-transfer excitons in TMD heterostructures. In twisted WSe_2/WSe_2 homobilayers, Xie *et al.* observed a pressure-induced dynamic tuning of moiré potentials and interlayer coupling strength, with moderate pressures (<7 GPa) continuously modulating hybridized charge-transfer excitonic states.[81] In particular, the interlayer excitons display a nonmonotonic evolution of photoluminescence (PL) spectra as a function of applied pressure, initially undergoing a red shift at low pressure, followed by a blue shift at a higher pressure. Similarly, interlayer excitons in TMD heterobilayers show strong dependence on pressure. For example, in WS_2/$MoSe_2$ heterobilayers, the application of pressure induces the transition of intralayer excitons into interlayer excitons due to enhanced interlayer coupling.[82] At high pressures, PL signatures from the intralayer excitons are quenched, and only interlayer excitonic signatures are visible, reflective of the full transition of intralayer excitons into interlayer excitons. Furthermore, the PL spectra for interlayer excitons red shifts upon applied pressure, which is attributed to the enhanced interlayer charge transfer and interlayer coupling strength, which modify exciton binding characteristics.[83] In a related study, Xia *et al.* observed a pressure-induced band changeover in WSe_2/$MoSe_2$ heterobilayers, as indicated by the nonmonotonic evolution of pressure-dependent PL of interlayer exciton (Fig. 5a and b).[84] In low pressures (<0.6 GPa), two PL peaks associated with the direct interlayer exciton (I_A) and with indirect interlayer exciton (I_B) show contrasting trends: I_A blue-shifts whereas the I_B red-shifts as a function of increasing pressure. At a higher pressure (>1 GPa), both peaks abruptly transition into higher energy peaks and now both peaks concurrently red-shift with increased pressure. First-principles calculations attribute this abrupt transition of interlayer exciton to the changeover of the electronic band structures upon pressure, which changes the valence band maximum position within the Brillouin zone. Further studies show that interlayer excitons universally exhibit a strong pressure dependence in other TMD heterobilayers, such as WSe_2/WS_2[85] and MoS_2/WS_2,[86] establishing pressure as an effective tuning parameter to control interlayer charge transfer and associated exciton dynamics in TMD heterostructures.

Beyond excitonic modulation and interlayer coupling, hydrostatic pressure induces profound changes in the electronic topology of vdW heterostructures, which prompts emergent quantum phases *via* pressure-driven interlayer charge transfer. In TaS_2-based systems, applied pressure can enhance interlayer coupling by reducing the vdW gap, which leads to enhanced orbital overlap between adjacent layers.[87–90] With further compression of the vdW gap, this enhanced coupling can drive electronic instabilities in TaS_2: suppression of charge-density waves, reconstruction of the Fermi surface, and emergence of supercon-
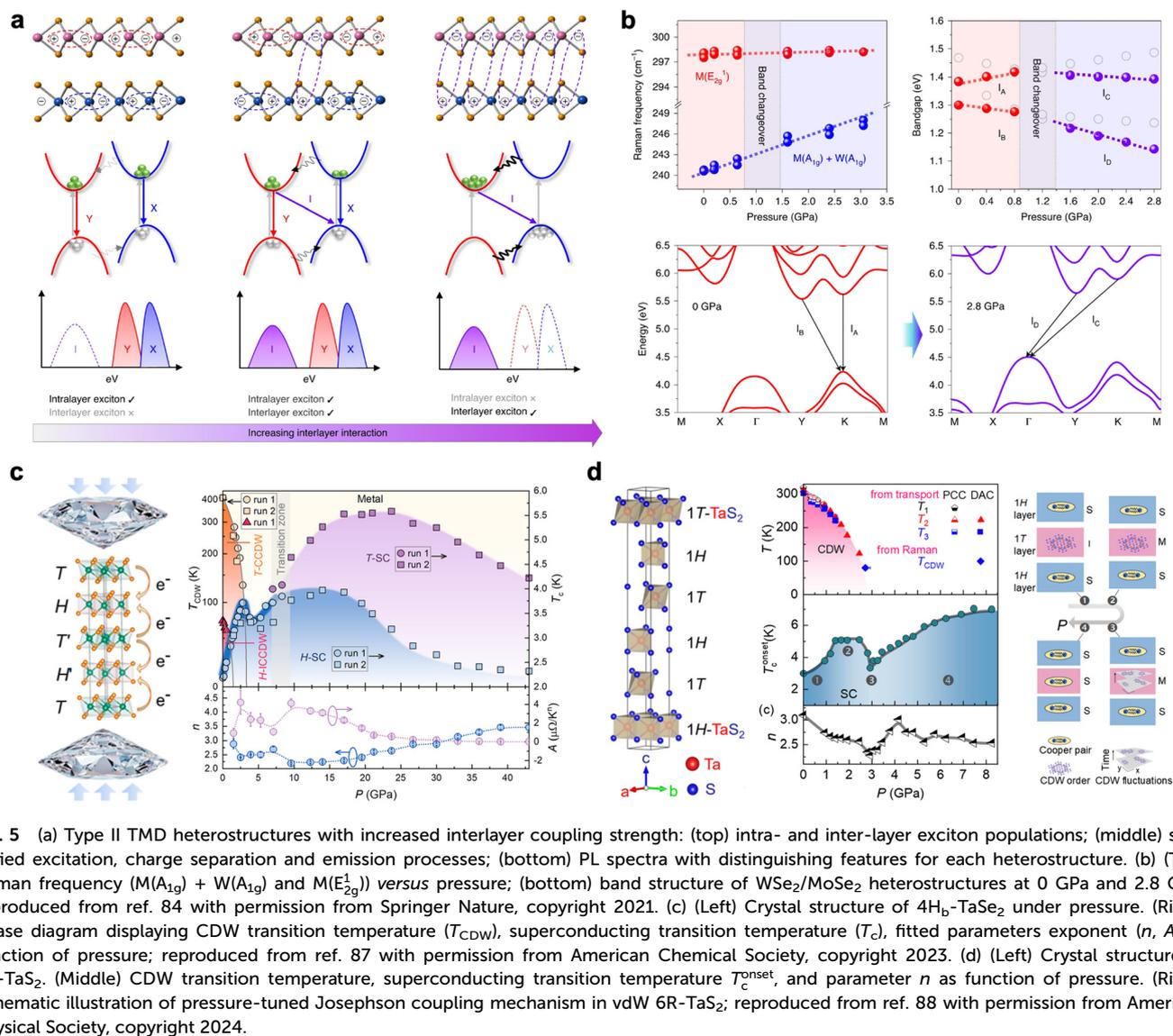
Fig. 5 (a) Type II TMD heterostructures with increased interlayer coupling strength: (top) intra- and inter-layer exciton populations; (middle) simplified excitation, charge separation and emission processes; (bottom) PL spectra with distinguishing features for each heterostructure. (b) (Top) Raman frequency (M(A_{1g}) + W(A_{1g}) and M(E_{2g}^1)) *versus* pressure; (bottom) band structure of WSe$_2$/MoSe$_2$ heterostructures at 0 GPa and 2.8 GPa; reproduced from ref. 84 with permission from Springer Nature, copyright 2021. (c) (Left) Crystal structure of 4H$_b$-TaSe$_2$ under pressure. (Right) Phase diagram displaying CDW transition temperature (T_{CDW}), superconducting transition temperature (T_c), fitted parameters exponent (n, A) as function of pressure; reproduced from ref. 87 with permission from American Chemical Society, copyright 2023. (d) (Left) Crystal structure of 6R-TaS$_2$. (Middle) CDW transition temperature, superconducting transition temperature T_c^{onset}, and parameter n as function of pressure. (Right) Schematic illustration of pressure-tuned Josephson coupling mechanism in vdW 6R-TaS$_2$; reproduced from ref. 88 with permission from American Physical Society, copyright 2024.

ductivity simultaneously arise from the pressure-induced crossover between weak to strong interlayer coupling regimes. Recent studies showed that pressure enhances interlayer electronic coupling in 4H$_b$-TaS$_2$ and drives charge transfer between TaS$_2$ layers.[87,89] Interestingly, Yan *et al.* demonstrated how superconductivity can be enhanced by applying pressure *via* the suppression of charge-density waves (CDWs), from which dual-superconductivity emerges (Fig. 5c).[87] Similarly, applied pressure induces a nonmonotonic evolution of superconductivity in 6R-TaS$_2$ *via* Lifshitz transition, which is attributed to the interlayer charge redistribution-driven Fermi surface reconstruction (Fig. 5d).[88,90] This pressure-induced modification of electronic structures, mediated by interlayer charge transfer, is also observed in other layered materials beyond TMDs. Lyubovskii *et al.* demonstrated that applying pressure to (BETS)$_4$CoBr$_4$ (DCB), a 2D layered metallic bilayer organic compound, significantly alters the interlayer charge transport and the electronic structure of the metallic layers.[91] Similarly, Zhu *et al.* reported that applying pressure to

2D oxide AgRuO$_3$ that crystallizes in a strongly correlated honeycomb lattice structure activates anomalous charge transfer between Au and Ru atoms, inducing a rare Ag^{2+} oxidation states within this compound.[92] This unusual charge transfer drives a sequence of insulator–metal–insulator transition together with a further structural phase transition at a larger pressure deep in the insulating state. These observations collectively suggest that pressure serves as an effective interlayer dopant, enabling dynamic modulation of interfacial charge transfer to mediate competing ground states in charge-transfer heterostructures.

4.   Applications of charge transfer

Charge-transfer polaritons

Polaritons are light–matter hybrid modes that enable extreme light confinement beyond the diffraction limit with enhanced light–matter interactions. Recently, the notion of charge-trans-

fer polariton has emerged as a new frontier to activate polaritonic response in 2D materials by controlling interlayer charge transfer. When combined with the exceptional tunability of 2D materials, these charge-transfer polaritons enable a wide range of polaritonic device design and serve as a fundamental probe of electrodynamics and light–matter interaction in the constituent materials. For example, Kim *et al.* demonstrated mid-infrared charged-transfer plasmons at the WO_x/graphene interface by oxidizing WSe_2/graphene into WO_x/graphene, which initiates charge-transfer doping of graphene due to the work-function mismatch as described above (Fig. 6a).[27] These plasmons exhibit plasmonic quality factor (Q_F) reaching the near-

intrinsic limit at room temperature, which is fundamentally limited by intrinsic electron–phonon scattering dominant at room temperatures. The imprinting of nanoscale graphene plasmonic cavities with laterally abrupt junctions was further demonstrated by locally creating nanoscale WO_x patterns on graphene. These latter WO_x patterns were created by selectively oxidizing the desired regions of WSe_2 placed on top of graphene using a pre-etched hBN as a mask layer prior to oxidation. By employing suspended structures of WO_x-encapsulated graphene, plasmonic whispering-gallery cavities with enhanced light–matter interactions were further realized. Similar charge-transfer plasmons have also been actively
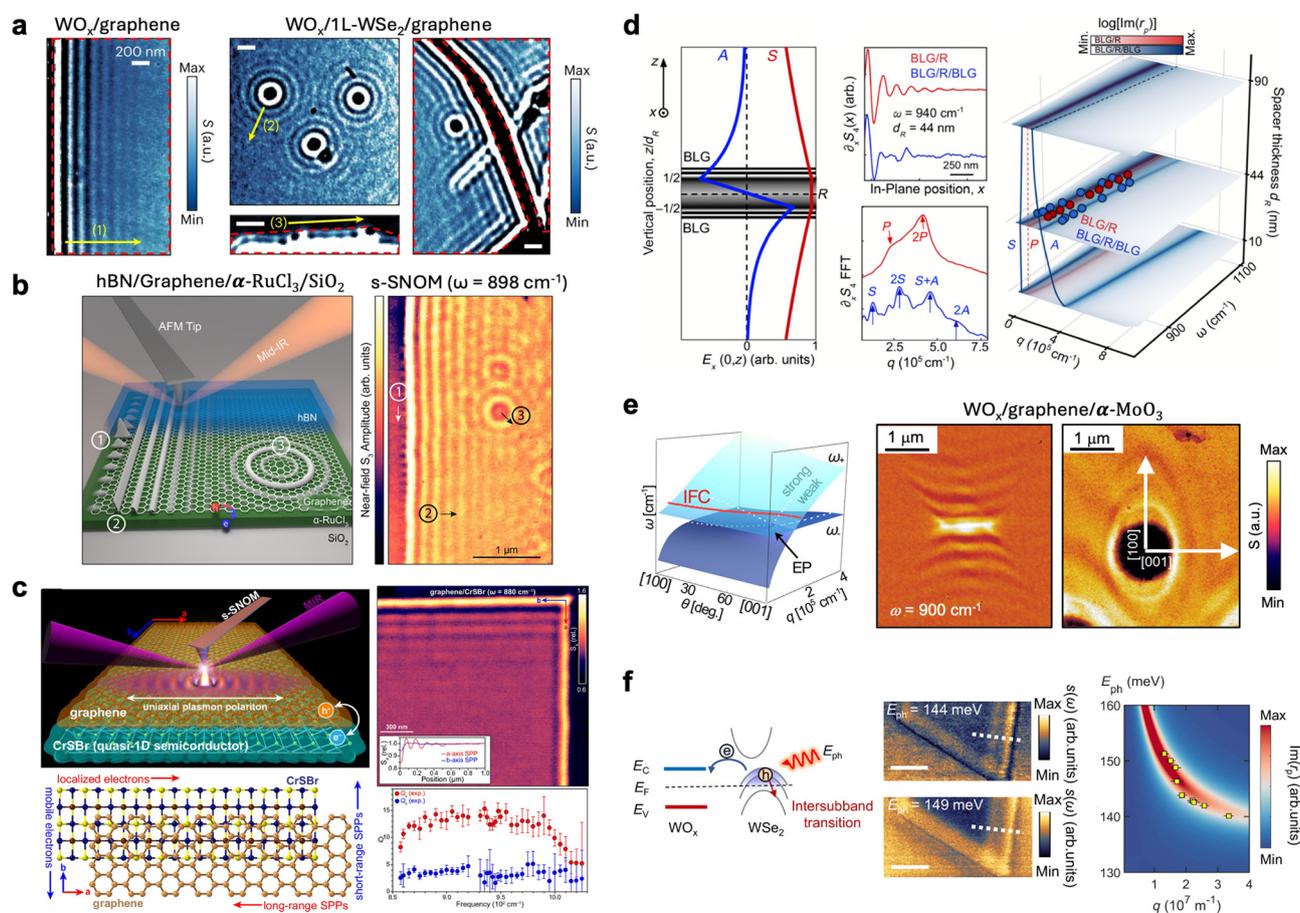

Fig. 6 Nano-infrared imaging of charge-transfer polaritons in (left) WO_x/graphene and (right) WO_x/1L-WSe_2/graphene measured at ambient conditions; adapted from ref. 27, with permission from Springer Nature. (b) (Left) Schematic of hBN/graphene/α-$RuCl_3$ heterostructures. (Right) Nano-infrared imaging of charge-transfer polaritons in hBN/graphene/α-$RuCl_3$ measured at cryogenic temperatures (T = 60 K); reproduced from ref. 93 with permission from American Chemical Society, copyright 2020. (c) (Top left) Schematic of graphene/CrSBr heterostructures. (Bottom left) Highly anisotropic crystal structure of CrSBr. (Top right) Nano-infrared imaging of charge-transfer polariton in the devices, and (bottom right) the extracted polaritonic quality factors; reproduced from ref. 96 with permission from Springer Nature, copyright 2025. (d) (Left) Calculated electric field profile of interlayer-coupled plasmons in multilayer graphene/α-$RuCl_3$ heterostructures. (Middle top) A linecut of nano-infrared images with polaritonic interference fringes. (Middle bottom) Corresponding Fourier components of plasmonic mode momentum. (Right) Dispersion diagram of interlayer-coupled plasmons; reproduced from ref. 32 with permission from American Physical Society, copyright 2025. (e) (Left) Dispersion diagram of coupled plasmon–phonon modes in WO_x/graphene/α-MoO_3 heterostructures as a function of q and θ, clearly revealing an exception point (EP). Nano-infrared images of (middle) hyperbolic phonon polaritons in α-MoO_3 and (right) coupled plasmon–phonon polaritons in WO_x/graphene/α-MoO_3 heterostructure. The change in the propagation wavefront reflects the topological transition of the polaritonic isofrequency contour; reproduced from ref. 97 with permission from Springer Nature, copyright 2022. (f) (Left) Diagram of charge transfer between WO_x and WSe_2 induced by the work-function mismatch. (Middle) Nano-infrared imaging and (right) dispersion diagram of the intersubband polaritons (ISP) in WO_x/4L-WSe_2 devices; reproduced from ref. 98 with permission from Springer Nature, copyright 2025.

studied in α-RuCl$_3$/graphene heterostructures. Here, plasmons arise from the large work-function α-RuCl$_3$ driving dominant hole transfer into the proximal graphene layer. For example, Rizzo et al. demonstrated mid-infrared plasmons in α-RuCl$_3$/graphene heterostructures with Q_F reaching as high as ~30 at cryogenic temperatures of 40 K (Fig. 6b).[93] In a related study, Q_F was found to further increase abruptly below 40 K, reaching as high as ~60 at 10 K.[94] This drastic increase at lower temperatures is attributed to the increase in the electron correlation-induced Mott gap in α-RuCl$_3$, demonstrating that charge-transfer polaritons serve as an effective probe of electron correlations in constituent materials. Vitalone et al. further showed clear resonant THz plasmonic signatures in α-RuCl$_3$/graphene cavities.[95] This study further revealed that Q_F of plasmons is highly dependent on the mode frequency and is particularly drastically reduced to ~1.5 at 1 THz. Moore et al. also observed interlayer-coupled plasmons with strong plasmon–plasmon coupling strengths in two few-layer graphene layers separated by a α-RuCl$_3$ spacer layer. In this latter structure, α-RuCl$_3$ layer also serves as a charge-transfer layer to activate plasmons in both the top and bottom multilayer graphene by prompting hole transfer (Fig. 6d).[32]

Since the initial observation of charge-transfer polaritons at the WO$_x$/graphene and α-RuCl$_3$/graphene interfaces, the scope of charge-transfer polaritons has rapidly expanded rapidly to encompass a much broader spectrum of material systems and applications. For example, Shen et al. reported charge-transfer plasmons in α-MoO$_3$/graphene by epitaxially growing a high work-function α-MoO$_3$ on graphene.[99] This is an interesting observation given that graphene plasmons have remained elusive in vdW assembled α-MoO$_3$/graphene heterostructures,[97] indicative of minimal charge transfer between α-MoO$_3$ and graphene. These contrasting results indicate the significance of the interfacial quality of α-MoO$_3$ in preserving its intrinsically large work-function. Rizzo et al. demonstrated that in graphene/CrSBr heterostructures, the charge-transfer plasmons in graphene strongly interacts with the electronic anisotropy in CrSBr (Fig. 6c).[96] As a result, otherwise isotropic graphene plasmons preferentially propagate parallel to the quasi-1D chains in the underlying CrSBr. The anisotropy ratio of Q_F for plasmons propagating parallel and perpendicular to the quasi-1D chains exceeds an order-of-magnitude. More recently, nanoscale molecular plasmonic cavities have been demonstrated by the self-assembly of C$_{60}$ arrays on graphene, which locally hole dopes the underlying graphene and directly defines the plasmonic cavity geometry.[100]

Charge-transfer polaritons also serve as a compelling platform to control light–matter coupling by interacting with other excitations that co-exist in the constituent materials. For example, Ruta et al. realized a topological transition of a hyperbolic isofrequency contour (IFC) of phonon polaritons in α-MoO$_3$ into a closed, elliptical IFC by coupling to the isotropic WO$_x$/graphene plasmons in the form of hybrid WO$_x$/graphene/α-MoO$_3$ heterostructures (Fig. 6e).[97] Careful studies further revealed that this coupled plasmon–phonon polaritons traverses an exceptional point (EP) when their in-plane propagation angle is continuously tuned. This EP crossing by propagation angle control is mediated by the angle-dependent electron–phonon coupling intrinsic to WO$_x$/graphene/α-MoO$_3$ structures. Thus, these observations uniquely establish a robust platform to study exceptional point physics based on polaritons. In a related study, Luo et al. reported the realization of hyperbolic intersubband polaritons in a few-layer WSe$_2$ by oxidizing the surface layer to induce interlayer charge transfer into the underlying WSe$_2$ (Fig. 6f).[98] This charge transfer renders a well-defined intersubband transitions with strong oscillator strengths by populating high energy subbands, enabling the formation of intersubband polaritons by coupling to free space photons. Nano-infrared imaging reveals signatures of hyperbolic intersubband polaritons, opening new avenues for exploring ultra-strong coupling physics and cavity electrodynamics based on 2D charge-transfer polaritonic cavities. Furthermore, Sternbach et al. reported the use of ultrafast light pulses to dynamically populate electron-hole pairs within WSe$_2$, which give rise to exotic nano-optical phenomena including electronic hyperbolicity with hyperbolic polaritons[101] as well as the bleaching and Stark shift of A-excitons.[102]

Charge-transfer transistor architectures

The control of interlayer charge transfer in vdW heterostructures has recently emerged as an effective strategy for enhancing the performance of 2D field-effect transistors (FETs). Band engineered interlayer charge transfer particularly offers multiple powerful functionalities. This includes the precise tuning of conductivity and mobility of the 2D channel as well as the engineering of the threshold voltage and electrical contacts while preserving the intrinsic properties of the 2D semiconductor channel. The key parameters for the state-of-the-art 2D devices with charge-transfer doping strategies are summarized in Table 1.[31,103–107] In contrast to conventional chemical doping that introduce detrimental dopant defects into the host lattice sites, the charge-transfer approach modu-

Table 1 Benchmarking key parameters for the state-of-the-art charge-transfer transistors

Materials	Methods	On/off ratio	R_c (kΩ μm)	Mobility (cm^2 V^{-1} s)	SS (mV dec^{-1})	I_{on} (μA μm^{-1})	Ref.
WO$_x$/WSe$_2$	Exfoliation	~10^9	4	108	350	280 (V_{DS} = −5 V, V_{GS} = −8 V)	103
WO$_x$/WSe$_2$	Exfoliation	>10^7	2.6	54	98	~100 (V_{DS} = −1.5 V, V_{GS} = −1.5 V)	104
WSe$_2$/α-RuCl$_3$/FLG	Exfoliation	~10^5	<2	1000 (RT); 80 000 (1.5 K)	7 (300 mK)	—	105
WO$_x$/WSe$_2$	Exfoliation	10^6	16	167	—	1.7 (V_{DS} = −1 V, V_{GS} = −100 V)	106
WSe$_2$/SnS$_2$	CVD	>10^7	0.041	64	—	1530 (V_{DS} = 0.94 V, V_{GS} = 60 V)	31
MoS$_2$/CrOCl	Exfoliation	10^6	8.8	425	—	300 (V_{DS} = 2 V, V_{GS} = −11 V)	107

lates carrier density through electrostatic charge redistribution across atomically sharp vdW interfaces, thereby avoiding structural damage and defect formation.[108]

A widely investigated interfacial charge-transfer approach in 2D FETs employs a high work-function WO_x layer. These layers are formed by oxidizing WSe_2 using UV-ozone treatment, which mainly serves as a stable p-type charge-transfer layer while preserving the intrinsic properties of the semiconductor channel. Choi et al. demonstrated that when a monolayer of WO_x is stacked on graphene, substantial hole transfer occurs, leading to low sheet resistance (R_{sh}) and the absence of a Dirac point in the transfer curves of graphene devices.[23] The extracted hole density and room-temperature mobility of WO_x/graphene reached up to 3×10^{13} cm^{-2} and 2000 cm^2 V^{-1} s^{-1}, respectively. The doping level can be effectively controlled by varying the layer number of WSe_2 spacer embedded between WO_x and graphene. With four layers of WSe_2 spacer, graphene mobility reaches as high as ~24 000 cm^2 V^{-1} s^{-1}, recovering

the near-intrinsic carrier mobility in graphene close to the electron–phonon limited mobility. These results indicate the high-quality nature of WO_x layer.

The high-quality 2D charge-transfer layers also offer exciting opportunities for engineering electrical contacts in 2D FETs. For example, the high hole density induced by WO_x can be utilized as contact spacer dopant to form seamless lateral junction transistors and improve contact resistance in 2D semiconductor-based devices. Ngo et al. employed electron-beam irradiation to selectively convert heavily doped WSe_2 channel area to lightly doped near the contact region and achieve low contact resistance (R_C) with controllable threshold voltage of the device (Fig. 7a).[103] This approach enabled hole-doped WSe_2 FETs with saturation current as high as 280 µA µm^{-1} and on/off ratio of ~10^9. In a related study, a 500 nm wide hBN layer was used as a mask layer for a WSe_2 channel to selectively oxidize the exposed WSe_2 area into WO_x and create a self-aligned top-gate structure laterally interfaced with doped
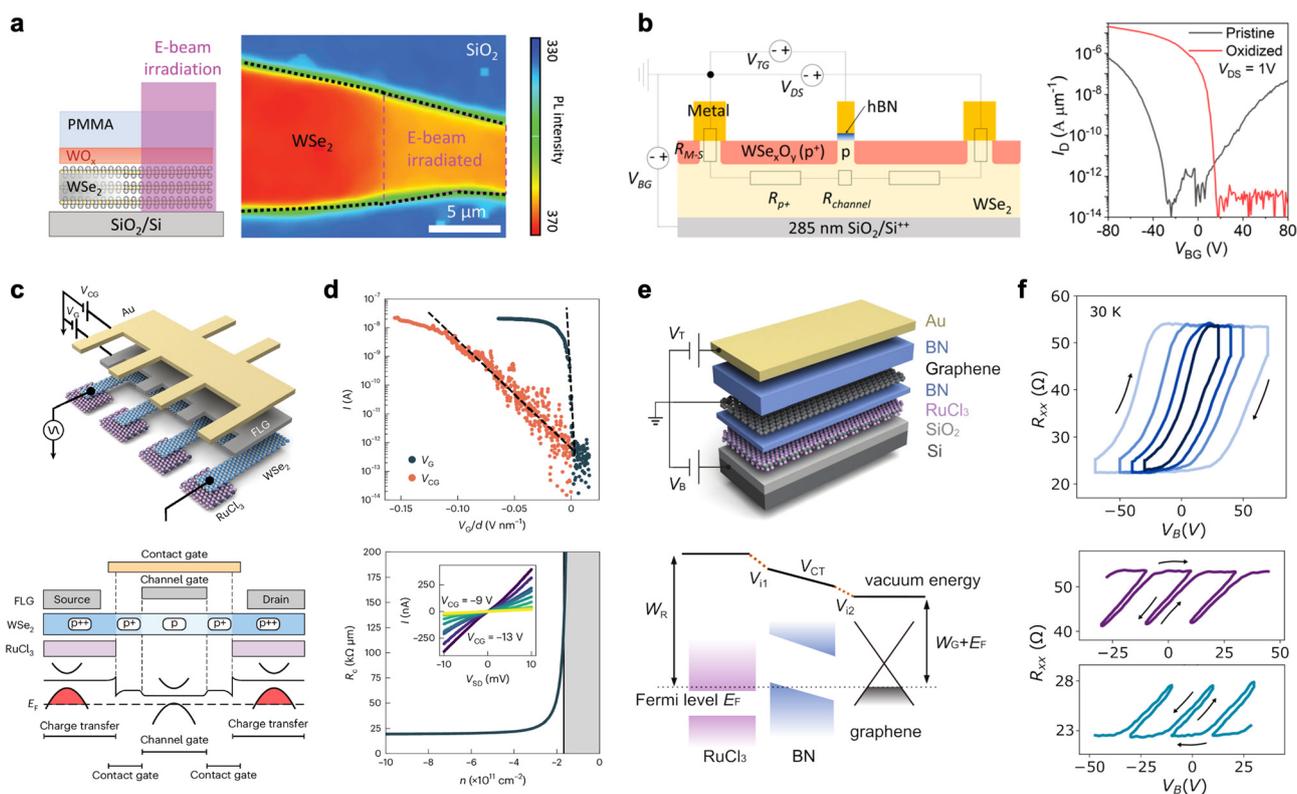

Fig. 7 (a) (Left) Schematic illustration of the WSe_2 device structure after UV-ozone oxidation, followed by e-beam irradiation on part of the device. (Right) PL intensity mapping of the e-beam-irradiated WSe_2 region, which shows uniform and weaker emission compared to that of the non-irradiated area; reproduced from ref. 103 with permission from John Wiley & Sons, copyright 2022. (b) (Left) Equivalent circuit diagram of the WSe_2 device, consisting of metal–semiconductor resistance (R_{M-S}), resistance of the heavily doped region (R_{p+}), and channel resistance ($R_{channel}$) connected in series. (Right) Transfer characteristics of the device before and after oxidation, which clearly demonstrate a transition from ambipolar to p-type behavior; reproduced from ref. 104 with permission from American Chemical Society, copyright 2023. (c) (Top) Schematic of the WSe_2 device structure featuring the WSe_2–$RuCl_3$ contact interface. (Bottom) Schematic of the corresponding doping profile and energy band diagram. (d) (Top) Gate response normalized by dielectric thickness as a function of channel gate voltage (V_G) and contact gate voltage (V_{CG}), used to compare the subthreshold slope. (Bottom) Contact resistance as a function of channel carrier density; reproduced from ref. 105 with permission from Springer Nature, copyright 2024. (e) (Top) Schematics of the device structure and (bottom) energy band diagram of the hysteretic $RuCl_3$/hBN/graphene charge-transfer heterostructure. (f) (Top) Bottom-gate (V_B) tunable hysteresis loop width and (bottom) the observed electronic ratchet effect; reproduced from ref. 109 under the terms of Attribution-NonCommercial-ShareAlike 4.0 International (CC BY-NC-SA 4.0).

contact regions (Fig. 7b).[104] A PMOS inverter was further demonstrated using this device architecture with a dramatically low power consumption of ~4.5 nW. Furthermore, Pack et al. showed that placing a patterned charge-transfer α-RuCl₃ layer on WSe₂ channel to hole dope the contact area enables robust electrical contacts that operate down to low temperatures and low channel carrier density of WSe₂ (Fig. 7c and d).[105] This new electrical contact architecture enabled the observation of record-high hole mobility of ~80 000 cm² V⁻¹ s⁻¹ as well as fractional quantum Hall effects in WSe₂. The concept of "hyper-doping" in WSe₂/SnS₂ heterostructures described above also enables extremely low contact resistance.[31] In these devices, the external electric fields applied via gate voltage dynamically modifies the band alignment, inducing ultrahigh carrier density ($\sim 1.5 \times 10^{14}$ cm⁻²) into WSe₂ and realizing an ultralow R_C of 41 Ω μm.

Finally, a new type of ferroelectric-like behavior has recently been discovered in graphene/hBN/α-RuCl₃ charge-transfer heterostructures, forming a robust and tunable interfacial dipole as a result of charge transfer between graphene and α-RuCl₃ (Fig. 7e and f).[109,110] In particular, these charge-transfer heterostructures display ferroelectric-like hysteresis loop that is robust against external magnetic field and operates at low temperatures. This behavior is attributed to the quantum exchange interaction at the hBN/α-RuCl₃ interface deforming local electronic orbitals and creating effective net interface dipole that is dynamically switchable by external gate. The origin of this ferroelectric-like response is fundamentally different from other reported classes of ferroelectrics that require a symmetry-breaking interface, thus opening a new paradigm to engineer hysteretic behaviors in 2D heterostructures via engineered interlayer charge transfer.

Photo- and electro-catalysis

The control of interlayer charge transfer in 2D materials dictates their surface chemical potential and reaction kinetics, representing a powerful strategy for engineering photo- and electro-chemical activities in energy applications. For example, Yu et al. recently investigated heterogeneous electrochemical charge transfer at the surface of twisted bilayer graphene, which is tuned by the interlayer moiré twist angle ranging between 0.22° and 5° (Fig. 8a and b).[111] To probe the interfacial electrochemical activity, a twisted bilayer graphene/hBN
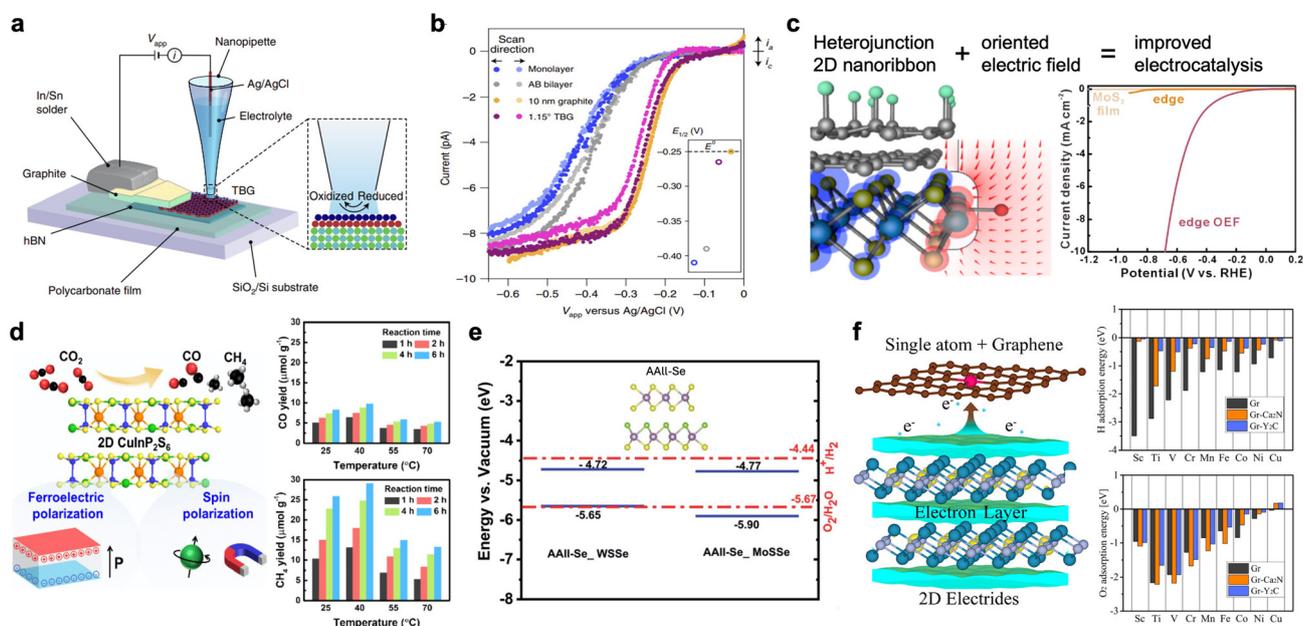

Fig. 8 (a) Schematic illustration of the scanning electrochemical cell microscopy (SECCM) setup equipped with a single-channel nanopipette probe (diameter ≈100 nm) mounted above the twisted bilayer graphene (TBG) surface for local voltammetric measurements. (b) Steady-state voltammograms of 2 mM Ru(NH₃)₆³⁺ in 0.1 M KCl solution measured on monolayer graphene, AB-stacked bilayer graphene, 10 nm graphite, and 1.15° TBG; reproduced from ref. 111 with permission from Springer Nature, copyright 2022. (c) Schematic representation of a heterojunction nanoribbon showing oriented electric fields (OEF) generated at the edge of 2D MoS₂, together with polarization curves of the MoS₂ flake, MoS₂ nanoribbon, and heterojunction nanoribbon; reproduced from ref. 112 with permission from American Chemical Society, copyright 2024. (d) Schematic diagram of 2D layered ferroelectric CIPS-mediated CO₂ reduction process. CO and CH₄ yields measured under photocatalytic CO₂ reduction at varying temperatures (25, 40, 55, and 70 °C) and reaction times (1, 2, 4, and 6 h); reproduced from ref. 113 with permission from American Chemical Society, 2024. (e) Band-edge positions of Janus TMDs relative to the vacuum level for two different heterojunctions, plotted against the redox potential of water splitting at pH = 0; reproduced from ref. 114 with permission from Royal Society of Chemistry, copyright 2022. (f) Schematic diagram of single-atom catalysis (SAC) heterostructures with 2D electride Ca₂N encapsulated within graphene. Comparison of the adsorption energies of H and O₂ atoms on graphene, Gr–Ca₂N, and Gr–Y₂C for various 3D transition-metal atoms; reproduced from ref. 115 with permission from American Chemical Society, copyright 2023.

heterostructure was fabricated and characterized using scanning electrochemical cell microscopy. Enhanced reaction kinetics and electrochemical charge transfer (comparable to that of 10 nm-thick graphite) was observed near the magic angle (1.15°), for which flat electronic bands emerge with maximized electronic density of states. In particular, the AA-stacked domains in magic-angle twisted bilayer graphene show anomalously enhanced electrochemical charge transfer beyond that expected from the enhancement of density of states from band flattening. The origin of this anomalous enhancement of electrochemical activity is yet to be uncovered, which sets a stage for future studies to shed light on how electronic flat-band topology and structural relaxation of 2D moiré heterostructures mediate and enhance interfacial electrochemical reactions.

Designing built-in electric fields in 2D heterostructures also serves as a powerful approach to engineer photo- and electro-catalytic activities. For example, Wang *et al.* studied fluorographene/MoS_2/graphene heterojunction nanoribbon to generate in-plane electric fields *via* the built-in electric dipole arising from the large work function difference.[112] In these structures, charge transfer induces oriented electric fields (OEFs) at the edges of 2D materials (Fig. 8c). Typical polarization curves in acidic solution showed that these OEFs in the heterojunction nanoribbons significantly increase the heterogeneous charge-transfer rate, resulting in a higher reaction current compared with pristine MoS_2 and MoS_2 nanoribbons. In a related study, Chiang *et al.* showed that ferroelectric semiconductors with intrinsic and switchable spontaneous electrical polarization, such as 2D $CuInP_2S_6$ (CIPS), serve as a robust platform to enhance the photocatalytic CO_2 reduction reaction (Fig. 8d).[113] The strong interlayer coupling in CIPS enables rapid interlayer charge transfer, which is crucial for improving its photocatalytic performance. Under an external magnetic field, the ferroelectric and spin polarizations of CIPS can be modulated, inducing directional band bending across the layers. This polarization-induced charge redistribution renders one surface electron rich and the opposite surface hole rich, thereby promoting efficient CO_2 adsorption and activation. In addition, the built-in polarization field enhances the separation of photogenerated carriers and effectively suppressing electron–hole recombination, leading to improved photocatalytic efficiency. Janus TMDs also hold promise in enhancing electrochemical activities owing to the inherent electric dipole formation. Recent DFT-based studies show that Janus TMD-based heterostructures, such as PtSSe/$ZrSe_2$ and MoSSe/WS_2, exhibit a combination of built-in electrical field and type II band alignment that result in favorable band edge positions for water splitting (Fig. 8e).[114,116,117] Other unique advantages of Janus TMDs include built-in electric field-driven efficient photoexcited electron–hole separation as well as high efficiency for capturing solar light.

Electride/graphene interface represents yet another promising charge-transfer heterostructure for regulating single-atom catalysis (SAC).[115] Based on DFT studies, Li *et al.* demonstrated that the catalytic activities toward the hydrogen evolution reaction (HER) and oxygen reduction reaction (ORR) were markedly enhanced at the electride/graphene interface due to efficient charge redistribution across the interface (Fig. 8f). In these heterostructures, Ca_2N or Y_2C—low-work-function 2D electrides—serve as electron-rich layered materials containing loosely bound anionic electrons. Here, graphene functions as a conductive, atomically thin charge-transfer mediator, enabling effective and continuous electron transfer from the electrides while simultaneously protecting them from environmental degradation. The substantial work-function difference between the electrides and graphene induces a high degree of electron transfer into the graphene layer. This excess charge is subsequently transferred to the supported single metal atoms, thereby modulating their electronic structures and enhancing their catalytic performance in SAC.

5. Outlook

The field of 2D materials has recently progressed to the level where the synthesis and assembly of 2D heterostructures can be controlled with ultrahigh precision. These exciting capabilities enable designer interlayer charge transfer between vdW layers, allowing the desired interfacial quantum properties to be engineered on demand.[118–121] Recent efforts have been expanding towards the interface between vdW and non-vdW materials.[122–125] This approach can potentially unlock a fundamentally new phase space for engineering interlayer charge transfer with the discovery of new emergent behavior[126] and applications.[127,128] A promising frontier is the integration of 2D materials with 3D single-crystalline complex transition metal oxides, which uniquely offer strongly correlated electronic degrees of freedom that drive emergent phenomena, ranging from high-temperature superconductivity to tunable magnetism.[9] The unique ionic nature of complex oxides particularly enables their work function to reach as high as ~7 eV by carefully controlling the surface termination layer with atomic precision.[129] Interfacing these high work-function oxides with 2D materials can induce extreme levels of charge transfer with an immediate impact in charge-transfer heterostructures for a wide range of fundamental studies and applications described above. In this respect, recent breakthroughs in preparing freestanding single-crystalline complex oxide membranes[130,131] offer tremendous opportunities to assemble these hybrid 2D/complex oxide membrane heterostructures.

However, the dangling bond on oxide surface is a formidable challenge as it promotes the formation of surface adsorbates, which can compromise the interfacial quality that is particularly critical to the interfacial charge transfer driven by work-function mismatch.[132] Accordingly, recent studies on 2D/oxide membrane heterostructures stacked in ambient conditions reveal a significant presence of interfacial contaminants.[133] Furthermore, the air sensitive nature of 2D/oxide interface poses another key challenge, since ambient exposure can trigger adatom adsorption–desorption dynamics that alter the work function of oxides, relax the charge-transfer state,

and ultimately deteriorate the doping stability.[134] These observations highlight the importance of forming well-defined, passivated 2D/oxide interfaces—through controlled oxidation, encapsulation, or the use of intrinsically passivating complex oxides—to preserve the desired electronic configuration over time.[28,135] We further note that the electrical properties of 2D/oxide charge-transfer transistors, particularly those consisting of oxidized 2D materials, are also governed by several extrinsic factors beyond the intrinsic work-function-mismatch mediated charge transfer at the interface. For example, oxidizing WSe_2 can produce non-stoichiometric WO_x depending on the oxidation conditions, which has been reported to give rise to defect states within the band gap.[136] The presence of these defect states can adversely affect device performance by increasing contact resistance *via* Fermi level pinning effects as well as reducing carrier mobility by introducing disorder-induced scattering pathways in channel materials.[26] In stacked charge-transfer devices, the presence of hydrocarbons confined in the form of interfacial "bubbles", combined with the non-stoichiometric nature of WO_x, can also locally perturb the magnitude of charge transfer, leading to detrimental doping density fluctuations in real space. One exciting future direction to address the challenges described above is to assemble these hybrid structures in ultra-high vacuum conditions to prevent the contamination of oxide surfaces.[17–19]

Another important consideration is the ability to visualize charge transfer dynamics at ultrafast timescale and with atomic resolution. This is particularly important for elucidating complex exciton dynamics and energy landscape in many TMD heterostructures. Recent advances in the experimental techniques have led to a rapid advancement in the mechanistic understanding of charge transfer and intra- and inter-layer exciton dynamics in TMD heterostructures. For example, ultrafast femtosecond electron diffraction technique has opened new avenues for visualizing and elucidating the salient role of phonon and lattice dynamics in interlayer exciton formation.[71] Similarly, femtosecond photoemission momentum microscopy enabled the visualization of exciton–phonon scattering as well as real-space aspects of the interlayer exciton wavefunction.[67,137,138] However, these approaches lack the ability to resolve local variations of excitonic and other electronic behavior at the atomic scale, which is critical for many physical phenomena observed in charge-transfer heterostructures. A promising frontier is light-assisted scanning probe microscopy techniques that couples light with nanoscale scanning probe tip to enable the imaging of ultrafast materials response deep beyond the diffraction limit.[139] One prominent example is scattering-type scanning near-field optical microscopy (s-SNOM) that operates over a broad range spanning THz to ultraviolet. When coupled with an ultrafast light source, s-SNOM enables simultaneous time- and spatially resolved nano-imaging of excitonic and polaritonic dynamics in 2D heterostructures.[101,102,140,141] Recent developments in ultrafast THz scanning tunneling microscopy further pushes the spatial resolution down to the angstrom scale.[142–145] Microwave impedance microscopy is yet another emerging approach that extends the ultrafast nanoscopy down to the GHz regime, which has recently shown promise in accessing depth-resolved charge-transfer dynamics in vdW heterostructures.[146–148] Looking ahead, the convergence of multi-modal microscopy (that integrates two or more modalities described above) with attosecond time-resolved techniques[149] is poised to push the frontier of charge transfer physics in 2D materials.

In conclusion, we discussed the rapid progress in programming interlayer charge transfer in vdW heterostructures by manipulating both structural and dynamic control parameters. These advances in engineering charge-transfer heterostructures have already led to breakthroughs across diverse application fronts, including polaritonic devices, transistor architectures, and photo- and electro-chemical cells. We are now witnessing the rapidly growing efforts towards integrating artificial intelligence and machine learning (AI/ML) into 2D materials research workflow and the next generation of charge-transfer heterostructure design.[150–165] For example, E. Gerber *et al.* developed InterMatch, a high-throughput computational framework that utilizes readily available 2D database to predict various interfacial parameters at 2D interfaces, including their charge transfer, strain profile, and superlattice structures.[158] This framework has proven useful in accelerating the design of 2D interface and heterostructures with tailored properties by overcoming the $O(N^3)$ scaling of the conventional density functional theory (DFT) in large N electron systems. Another important consideration is the accuracy of these predictions compared to experimental observations. In this regard, the accuracy of InterMatch has shown to be comparable to or better than that of DFT. One emerging direction to further improve the calculation accuracy is to use machine learning-based force fields (MLFF), which models interatomic interactions by directly training ML algorithms from quantum-mechanical calculations.[166] These MLFF demonstrate a quantum-level accuracy while maintaining the desired computational efficiency for large-scale systems. The other emerging powerful approach to close the theory–experiment gap is to establish a AI/ML-driven self-driving laboratory (SDL) that combines both theoretical and experimental procedures.[167] Recent studies have demonstrated AI/ML-based automation of key experimental protocols for assembling and characterizing 2D heterostructures.[19,167–173] Moving forward, we envision that combining the currently disconnected AI/ML-based efforts in theoretical and experimental approaches into a closed-loop, Level 5 SDL without human-in-the-loop steps will further accelerate the discovery of yet untapped phenomena and functionalities in charge-transfer vdW heterostructures.[173] Taken together, the design of interlayer charge transfer in vdW heterostructures, combined with AI/ML-driven approaches, holds tremendous potential for growth and impact in fundamental studies and technologies for years to come.

Conflicts of interest

There are no conflicts to declare.

Data availability

Acknowledgements

References

1 R. Dingle, H. L. Störmer, A. C. Gossard and W. Wiegmann, *Appl. Phys. Lett.*, 1978, **33**, 665–667.

2 O. Ambacher, J. Smart, J. R. Shealy, N. G. Weimann, K. Chu, M. Murphy, W. J. Schaff, L. F. Eastman, R. Dimitrov, L. Wittmer, M. Stutzmann, W. Rieger and J. Hilsenbeck, *J. Appl. Phys.*, 1999, **85**, 3222–3233.

3 F. Capasso, *Science*, 1987, **235**, 172–176.

4 T. Ando, A. B. Fowler and F. Stern, *Rev. Mod. Phys.*, 1982, **54**, 437–672.

5 A. Ohtomo and H. Y. Hwang, *Nature*, 2004, **427**, 423–426.

6 N. Nakagawa, H. Y. Hwang and D. A. Muller, *Nat. Mater.*, 2006, **5**, 204–209.

7 J. Mannhart and D. G. Schlom, *Science*, 2010, **327**, 1607–1611.

8 P. Zubko, S. Gariglio, M. Gabay, P. Ghosez and J.-M. Triscone, *Annu. Rev. Condens. Matter Phys.*, 2011, **2**, 141–165.

9 H. Y. Hwang, Y. Iwasa, M. Kawasaki, B. Keimer, N. Nagaosa and Y. Tokura, *Nat. Mater.*, 2012, **11**, 103–113.

10 S. Stemmer and S. J. Allen, *Annu. Rev. Mater. Res.*, 2014, **44**, 151–171.

11 A. K. Geim and I. V. Grigorieva, *Nature*, 2013, **499**, 419–425.

12 K. S. Novoselov, A. K. Geim, S. V. Morozov, D. Jiang, M. I. Katsnelson, I. V. Grigorieva, S. V. Dubonos and A. A. Firsov, *Nature*, 2005, **438**, 197–200.

13 R. Decker, Y. Wang, V. W. Brar, W. Regan, H.-Z. Tsai, Q. Wu, W. Gannett, A. Zettl and M. F. Crommie, *Nano Lett.*, 2011, **11**, 2291–2295.

14 D. Rhodes, S. H. Chae, R. Ribeiro-Palau and J. Hone, *Nat. Mater.*, 2019, **18**, 541–549.

15 L. Wang, I. Meric, P. Y. Huang, Q. Gao, Y. Gao, H. Tran, T. Taniguchi, K. Watanabe, L. M. Campos, D. A. Muller, J. Guo, P. Kim, J. Hone, K. L. Shepard and C. R. Dean, *Science*, 2013, **342**, 614–617.

16 F. Pizzocchero, L. Gammelgaard, B. S. Jessen, J. M. Caridad, L. Wang, J. Hone, P. Bøggild and T. J. Booth, *Nat. Commun.*, 2016, **7**, 11894.

17 S. Guo, M. Luo, G. Shi, N. Tian, Z. Huang, F. Yang, L. Ma, N. Z. Wang, Q. Shi, K. Xu, Z. Xu, K. Watanabe, T. Taniguchi, X. H. Chen, D. Shen, L. Zhang, W. Ruan and Y. Zhang, *Rev. Sci. Instrum.*, 2023, **94**, 013903.

18 W. Wang, N. Clark, M. Hamer, A. Carl, E. Tovari, S. Sullivan-Allsop, E. Tillotson, Y. Gao, H. de Latour, F. Selles, J. Howarth, E. G. Castanon, M. Zhou, H. Bai, X. Li, A. Weston, K. Watanabe, T. Taniguchi, C. Mattevi, T. H. Bointon, P. V. Wiper, A. J. Strudwick, L. A. Ponomarenko, A. V. Kretinin, S. J. Haigh, A. Summerfield and R. Gorbachev, *Nat. Electron.*, 2023, **6**, 981–990.

19 A. J. Mannix, A. Ye, S. H. Sung, A. Ray, F. Mujid, C. Park, M. Lee, J.-H. Kang, R. Shreiner, A. A. High, D. A. Muller, R. Hovden and J. Park, *Nat. Nanotechnol.*, 2022, **17**, 361–366.

20 C. R. Dean, A. F. Young, I. Meric, C. Lee, L. Wang, S. Sorgenfrei, K. Watanabe, T. Taniguchi, P. Kim, K. L. Shepard and J. Hone, *Nat. Nanotechnol.*, 2010, **5**, 722–726.

21 A. A. Zibrov, C. Kometter, H. Zhou, E. M. Spanton, T. Taniguchi, K. Watanabe, M. P. Zaletel and A. F. Young, *Nature*, 2017, **549**, 360–364.

22 J. I. A. Li, C. Tan, S. Chen, Y. Zeng, T. Taniguchi, K. Watanabe, J. Hone and C. R. Dean, *Science*, 2017, **358**, 648–652.

23 M. S. Choi, A. Nipane, B. S. Y. Kim, M. E. Ziffer, I. Datta, A. Borah, Y. Jung, B. Kim, D. Rhodes, A. Jindal, Z. A. Lamport, M. Lee, A. Zangiabadi, M. N. Nair, T. Taniguchi, K. Watanabe, I. Kymissis, A. N. Pasupathy, M. Lipson, X. Zhu, W. J. Yoo, J. Hone and J. T. Teherani, *Nat. Electron.*, 2021, **4**, 731–739.

24 M. Yamamoto, S. Dutta, S. Aikawa, S. Nakaharai, K. Wakabayashi, M. S. Fuhrer, K. Ueno and K. Tsukagoshi, *Nano Lett.*, 2015, **15**, 2067–2073.

25 B. S. Y. Kim, T. D. Ngo, Y. Hassan, S. H. Chae, S. G. Yoon and M. S. Choi, *Adv. Sci.*, 2024, **11**, 2407175.

26 X. Liu, M. S. Choi, E. Hwang, W. J. Yoo and J. Sun, *Adv. Mater.*, 2022, **34**, 2108425.

27 B. S. Y. Kim, A. J. Sternbach, M. S. Choi, Z. Sun, F. L. Ruta, Y. Shao, A. S. McLeod, L. Xiong, Y. Dong, T. S. Chung, A. Rajendran, S. Liu, A. Nipane, S. H. Chae, A. Zangiabadi, X. Xu, A. J. Millis, P. J. Schuck, C. R. Dean, J. C. Hone and D. N. Basov, *Nat. Mater.*, 2023, **22**, 838–843.

28 K. Lee, B. S. Y. Kim, M. S. Choi, N. Ali, H. Shin, D. Yue, G. H. Kim, J. Hone and W. J. Yoo, *ACS Appl. Electron. Mater.*, 2024, **6**, 3894–3900.

29 T. Huynh, T. D. Ngo, H. Choi, M. Choi, W. Lee, T. D. Nguyen, T. T. Tran, K. Lee, J. Y. Hwang, J. Kim and W. J. Yoo, *ACS Appl. Mater. Interfaces*, 2024, **16**, 3694–3702.

30 Y. Wang, J. Balgley, E. Gerber, M. Gray, N. Kumar, X. Lu, J.-Q. Yan, A. Fereidouni, R. Basnet, S. J. Yun, D. Suri, H. Kitadai, T. Taniguchi, K. Watanabe, X. Ling, J. Moodera, Y. H. Lee, H. O. H. Churchill, J. Hu, L. Yang, E.-A. Kim, D. G. Mandrus, E. A. Henriksen and K. S. Burch, *Nano Lett.*, 2020, **20**, 8446–8452.

31 B. Zhao, Z. Zhang, J. Xu, D. Guo, T. Gu, G. He, P. Lu, K. He, J. Li, Z. Chen, Q. Ren, L. Miao, J. Lu, Z. Ni, X. Duan and X. Duan, *Science*, 2025, **388**, 1183–1188.

32 S. L. Moore, M. S. Sánchez, M. C. Strasbourg, Y. Shao, J. Pack, Y. Wang, D. J. Rizzo, B. S. Jessen, M. Cothrine, D. G. Mandrus, T. Taniguchi, K. Watanabe, K. S. Burch, C. R. Dean, J. Hone, M. Fogler, A. J. Millis, A. Rubio, P. J. Schuck, T. Stauber and D. N. Basov, *Phys. Rev. X*, 2025, **15**, 041011.

33 D. Lee, J. J. Lee, Y. S. Kim, Y. H. Kim, J. C. Kim, W. Huh, J. Lee, S. Park, H. Y. Jeong, Y. D. Kim and C.-H. Lee, *Nat. Electron.*, 2021, **4**, 664–670.

34 B. Matta, P. Rosenzweig, C. Polley, U. Starke and K. Küster, *Nanoscale*, 2025, **17**, 19317.

35 A. Mishchenko, J. S. Tu, Y. Cao, R. V. Gorbachev, J. R. Wallbank, M. T. Greenaway, V. E. Morozov, S. V. Morozov, M. J. Zhu, S. L. Wong, F. Withers, C. R. Woods, Y.-J. Kim, K. Watanabe, T. Taniguchi, E. E. Vdovin, O. Makarovsky, T. M. Fromhold, V. I. Fal'ko, A. K. Geim, L. Eaves and K. S. Novoselov, *Nat. Nanotechnol.*, 2014, **9**, 808–813.

36 P. K. Srivastava, Y. Hassan, D. J. P. de Sousa, Y. Gebredingle, M. Joe, F. Ali, Y. Zheng, W. J. Yoo, S. Ghosh, J. T. Teherani, B. Singh, T. Low and C. Lee, *Nat. Electron.*, 2021, **4**, 269–276.

37 Z. Zhang, B. Zhang, Y. Wang, M. Wang, Y. Zhang, H. Li, J. Zhang and A. Song, *Nano Lett.*, 2023, **23**, 8132–8139.

38 Z. Zheng, Q. Ma, Z. Bi, S. de la Barrera, M.-H. Liu, N. Mao, Y. Zhang, N. Kiper, K. Watanabe, T. Taniguchi, J. Kong, W. A. Tisdale, R. Ashoori, N. Gedik, L. Fu, S.-Y. Xu and P. Jarillo-Herrero, *Nature*, 2020, **588**, 71–76.

39 R. Niu, Z. Li, X. Han, Z. Qu, D. Ding, Z. Wang, Q. Liu, T. Liu, C. Han, K. Watanabe, T. Taniguchi, M. Wu, Q. Ren, X. Wang, J. Hong, J. Mao, Z. Han, K. Liu, Z. Gan and J. Lu, *Nat. Commun.*, 2022, **13**, 6241.

40 K. Yasuda, X. Wang, K. Watanabe, T. Taniguchi and P. Jarillo-Herrero, *Science*, 2021, **372**, 1458–1462.

41 M. V. Stern, Y. Waschitz, W. Cao, I. Nevo, K. Watanabe, T. Taniguchi, E. Sela, M. Urbakh, O. Hod and M. Ben Shalom, *Science*, 2021, **372**, 1462–1466.

42 C. R. Woods, P. Ares, H. Nevison-Andrews, M. J. Holwill, R. Fabregas, F. Guinea, A. K. Geim, K. S. Novoselov, N. R. Walet and L. Fumagalli, *Nat. Commun.*, 2021, **12**, 347.

43 S. L. Moore, C. J. Ciccarino, D. Halbertal, L. J. McGilly, N. R. Finney, K. Yao, Y. Shao, G. Ni, A. Sternbach, E. J. Telford, B. S. Kim, S. E. Rossi, K. Watanabe, T. Taniguchi, A. N. Pasupathy, C. R. Dean, J. Hone, P. J. Schuck, P. Narang and D. N. Basov, *Nat. Commun.*, 2021, **12**, 5741.

44 X. Wang, K. Yasuda, Y. Zhang, S. Liu, K. Watanabe, T. Taniguchi, J. Hone, L. Fu and P. Jarillo-Herrero, *Nat. Nanotechnol.*, 2022, **17**, 367–371.

45 A. Weston, E. G. Castanon, V. Enaldiev, F. Ferreira, S. Bhattacharjee, S. Xu, H. Corte-León, Z. Wu, N. Clark, A. Summerfield, T. Hashimoto, Y. Gao, W. Wang, M. Hamer, H. Read, L. Fumagalli, A. V. Kretinin, S. J. Haigh, O. Kazakova, A. K. Geim, V. I. Fal'ko and R. Gorbachev, *Nat. Nanotechnol.*, 2022, **17**, 390–395.

46 L. Rogée, L. Wang, Y. Zhang, S. Cai, P. Wang, M. Chhowalla, W. Ji and S. P. Lau, *Science*, 2022, **376**, 973–978.

47 Y. Hassan, B. Singh, M. Joe, B. M. Son, T. D. Ngo, Y. Jang, S. Sett, A. Singha, R. Biswas, M. Bhakar, K. Watanabe, T. Taniguchi, V. Raghunathan, G. Sheet, Z. Lee, W. J. Yoo, P. K. Srivastava and C. Lee, *Adv. Mater.*, 2024, **36**, 2406290.

48 S. Deb, W. Cao, N. Raab, K. Watanabe, T. Taniguchi, M. Goldstein, L. Kronik, M. Urbakh, O. Hod and M. B. Shalom, *Nature*, 2022, **612**, 465–469.

49 K. Yasuda, E. Zalys-Geller, X. Wang, D. Bennett, S. S. Cheema, K. Watanabe, T. Taniguchi, E. Kaxiras, P. Jarillo-Herrero and R. Ashoori, *Science*, 2024, **385**, 53–56.

50 Y. Yeo, Y. Sharaby, N. Roy, N. Raab, K. Watanabe, T. Taniguchi and M. B. Shalom, *Nature*, 2025, **638**, 389–393.

51 A. Y. Lu, H. Zhu, J. Xiao, C. P. Chuu, Y. Han, M. H. Chiu, C. C. Cheng, C. W. Yang, K. H. Wei, Y. M. Yang, Y. Wang, D. Sokaras, D. Nordlund, P. Yang, D. A. Muller, M. Y. Chou, X. Zhang and L. J. Li, *Nat. Nanotechnol.*, 2017, **12**, 744–749.

52 K. Zhang, Y. Guo, D. T. Larson, Z. Zhu, S. Fang, E. Kaxiras, J. Kong and S. Huang, *ACS Nano*, 2021, **15**, 14394–14403.

53 T. Zheng, Y.-C. Lin, Y. Yu, P. Valencia-Acuna, A. A. Puretzky, R. Torsi, C. Liu, I. N. Ivanov, G. Duscher, D. B. Geohegan, Z. Ni, K. Xiao and H. Zhao, *Nano Lett.*, 2021, **21**, 931–937.

54 J. Zhang, S. Jia, I. Kholmanov, L. Dong, D. Er, W. Chen, H. Guo, Z. Jin, V. B. Shenoy, L. Shi and J. Lou, *ACS Nano*, 2017, **11**, 8192–8198.

55 D. B. Trivedi, G. Turgut, Y. Qin, M. Y. Sayyad, D. Hajra, M. Howell, L. Liu, S. Yang, N. H. Patoary, H. Li, M. M. Petrić, M. Meyer, M. Kremser, M. Barbone, G. Soavi, A. V. Stier, K. Müller, S. Yang, I. S. Esqueda, H. Zhuang, J. J. Finley and S. Tongay, *Adv. Mater.*, 2020, **32**, 2006320.

56 T. Zheng, Y.-C. Lin, N. Rafizadeh, D. B. Geohegan, Z. Ni, K. Xiao and H. Zhao, *ACS Nano*, 2022, **16**, 4197–4205.

57 X. Hong, J. Kim, S.-F. Shi, Y. Zhang, C. Jin, Y. Sun, S. Tongay, J. Wu, Y. Zhang and F. Wang, *Nat. Nanotechnol.*, 2014, **9**, 682–686.

58 P. Rivera, H. Yu, K. L. Seyler, N. P. Wilson, W. Yao and X. Xu, *Nat. Nanotechnol.*, 2018, **13**, 1004–1015.

59 B. Miller, A. Steinhoff, B. Pano, J. Klein, F. Jahnke, A. Holleitner and U. Wurstbauer, *Nano Lett.*, 2017, **17**, 5229–5237.

60 J. R. Schaibley, P. Rivera, H. Y. Yu, K. L. Seyler, J. Q. Yan, D. G. Mandrus, T. Taniguchi, K. Watanabe, W. Yao and X. D. Xu, *Nat. Commun.*, 2016, **7**, 13747.

61 P. Rivera, J. R. Schaibley, A. M. Jones, J. S. Ross, S. Wu, G. Aivazian, P. Klement, K. Seyler, G. Clark, N. J. Ghimire, J. Yan, D. G. Mandrus, W. Yao and X. D. Xu, *Nat. Commun.*, 2015, **6**, 6242.

62 H. Fang, C. Battaglia, C. Carraro, S. Nemsak, B. Ozdol, J. S. Kang, H. A. Bechtel, S. B. Desai, F. Kronast, A. A. Unal, G. Conti, C. Conlon, G. K. Palsson, M. C. Martin, A. M. Minor, C. S. Fadley, E. Yablonovitch, R. Maboudian and A. Javey, *Proc. Natl. Acad. Sci. U. S. A.*, 2014, **111**, 6198–6202.

63 J. Kunstmann, F. Mooshammer, P. Nagler, A. Chaves, F. Stein, N. Paradiso, G. Plechinger, C. Strunk, C. Schüller, G. Seifert, D. R. Reichman and T. Korn, *Nat. Phys.*, 2018, **14**, 801–805.

64 J. Kim, C. Jin, B. Chen, H. Cai, T. Zhao, P. Lee, S. Kahn, K. Watanabe, T. Taniguchi, S. Tongay, M. F. Crommie and F. Wang, *Sci. Adv.*, 2017, **3**, e1700518.

65 J. R. Schaibley, H. Yu, G. Clark, P. Rivera, J. S. Ross, K. L. Seyler, W. Yao and X. Xu, *Nat. Rev. Mater.*, 2016, **1**, 16055.

66 K. F. Mak and J. Shan, *Nat. Nanotechnol.*, 2022, **17**, 686–695.

67 D. Schmitt, J. P. Bange, W. Bennecke, A. AlMutairi, G. Meneghini, K. Watanabe, T. Taniguchi, D. Steil, D. R. Luke, R. T. Weitz, S. Steil, G. S. M. Jansen, S. Brem, E. Malic, S. Hofmann, M. Reutzel and S. Mathias, *Nature*, 2022, **608**, 499–503.

68 Z. Wang, D. A. Rhodes, K. Watanabe, T. Taniguchi, J. C. Hone, J. Shan and K. F. Mak, *Nature*, 2019, **574**, 76–80.

69 V. R. Policht, H. Mittenzwey, O. Dogadov, M. Katzer, A. Villa, Q. Li, B. Kaiser, A. M. Ross, F. Scotognella, X. Zhu, A. Knorr, M. Selig, G. Cerullo and S. Dal Conte, *Nat. Commun.*, 2023, **14**, 7273.

70 J. Wagner, R. Bernhardt, L. Rieland, O. Abdul-Aziz, Q. Li, X. Zhu, S. Dal Conte, G. Cerullo, P. H. M. van Loosdrecht and H. Hedayat, *Adv. Opt. Mater.*, 2025, **13**, 2402703.

71 A. Sood, J. B. Haber, J. Carlström, E. A. Peterson, E. Barre, J. D. Georgaras, A. H. M. Reid, X. Shen, M. E. Zajac, E. C. Regan, J. Yang, T. Taniguchi, K. Watanabe, F. Wang, X. Wang, J. B. Neaton, T. F. Heinz, A. M. Lindenberg, F. H. da Jornada and A. Raja, *Nat. Nanotechnol.*, 2023, **18**, 29–35.

72 L. Ma, P. X. Nguyen, Z. Wang, Y. Zeng, K. Watanabe, T. Taniguchi, A. H. MacDonald, K. F. Mak and J. Shan, *Nature*, 2021, **598**, 585–589.

73 J. Gu, L. Ma, S. Liu, K. Watanabe, T. Taniguchi, J. C. Hone, J. Shan and K. F. Mak, *Nat. Phys.*, 2022, **18**, 395–400.

74 X. Sun, Y. Zhu, H. Qin, B. Liu, Y. Tang, T. Lü, S. Rahman, T. Yildirim and Y. Lu, *Nature*, 2022, **610**, 478–484.

75 K. L. Seyler, P. Rivera, H. Yu, N. P. Wilson, E. L. Ray, D. G. Mandrus, J. Yan, W. Yao and X. Xu, *Nature*, 2019, **567**, 66–70.

76 K. Tran, G. Moody, F. Wu, X. Lu, J. Choi, K. Kim, A. Rai, D. A. Sanchez, J. Quan, A. Singh, J. Embley, A. Zepeda, M. Campbell, T. Autry, T. Taniguchi, K. Watanabe, N. Lu, S. K. Banerjee, K. L. Silverman, S. Kim, E. Tutuc, L. Yang, A. H. MacDonald and X. Li, *Nature*, 2019, **567**, 71–75.

77 E. M. Alexeev, D. A. Ruiz-Tijerina, M. Danovich, M. J. Hamer, D. J. Terry, P. K. Nayak, S. Ahn, S. Pak, J. Lee, J. I. Sohn, M. R. Molas, M. Koperski, K. Watanabe, T. Taniguchi, K. S. Novoselov, R. V. Gorbachev, H. S. Shin, V. I. Fal'ko and A. I. Tartakovskii, *Nature*, 2019, **567**, 81–86.

78 C. Jin, E. C. Regan, A. Yan, M. I. B. Utama, D. Wang, S. Zhao, Y. Qin, S. Yang, Z. Zheng, S. Shi, K. Watanabe, T. Taniguchi, S. Tongay, A. Zettl and F. Wang, *Nature*, 2019, **567**, 76–80.

79 J. Kumlin, A. Srivastava and T. Pohl, *Phys. Rev. Lett.*, 2025, **134**, 126901.

80 L. Zhang, Y. Tang, A. R. Khan, M. M. Hasan, P. Wang, H. Yan, T. Yildirim, J. F. Torres, G. P. Neupane, Y. Zhang, Q. Li and Y. Lu, *Adv. Sci.*, 2020, **7**, 2002697.

81 X. Xie, J. Ding, B. Wu, H. Zheng, S. Li, C.-T. Wang, J. He, Z. Liu, J.-T. Wang and Y. Liu, *Nano Lett.*, 2023, **23**, 8833–8841.

82 X. Ma, S. Fu, J. Ding, M. Liu, A. Bian, F. Hong, J. Sun, X. Zhang, X. Yu and D. He, *Nano Lett.*, 2021, **21**, 8035–8042.

83 J. Fan, J. Song, Y. Cheng and M. Sun, *Results Phys.*, 2021, **24**, 104110.

84 J. Xia, J. Yan, Z. Wang, Y. He, Y. Gong, W. Chen, T. C. Sum, Z. Liu, P. M. Ajayan and Z. Shen, *Nat. Phys.*, 2021, **17**, 92–98.

85 M. Zhu, Z. Zhang, T. Zhang, D. Liu, H. Zhang, Z. Zhang, Z. Li, Y. Cheng and W. Huang, *Nano Lett.*, 2022, **22**, 4528–4534.

86 J.-S. Kim, N. Maity, M. Kim, S. Fu, R. Juneja, A. Singh, D. Akinwande and J.-F. Lin, *ACS Appl. Mater. Interfaces*, 2022, **14**, 46841–46849.

87 L. Yan, C. Ding, M. Li, R. Tang, W. Chen, B. Liu, K. Bu, T. Huang, D. Dai, X. Jin, X. Yang, E. Cheng, N. Li, Q. Zhang, F. Liu, X. Liu, D. Zhang, S. Ma, Q. Tao, P. Zhu, S. Li, X. Lü, J. Sun, X. Wang and W. Yang, *Nano Lett.*, 2023, **23**, 2121–2128.

88 S. Wang, Y. Han, S. Sun, S. Wang, C. An, C. Chen, L. Zhang, Y. Zhou, J. Zhou and Z. Yang, *Phys. Rev. Lett.*, 2024, **133**, 056001.

89 R. M. Roy, X. Feng, M. Wenzel, V. Hasse, C. Shekhar, M. G. Vergniory, C. Felser, A. V. Pronin and M. Dressel, *Phys. Rev. Lett.*, 2025, **135**, 116503.

90 X. Lv, H. Song, K. Chen, S. Liu, Y. Huang, Y. Fang, Z. Shen and T. Cui, *Sci. China: Phys., Mech. Astron.*, 2024, **67**, 128211.

91 R. B. Lyubovskii, S. I. Pesotskii, V. N. Zverev, E. I. Zhilyaeva, A. M. Flakina and R. N. Lyubovskaya, *JETP Lett.*, 2021, **133**, 104–108.

92 C. Zhu, J. Yang, P. Shan, M.-H. Zhao, S. Zhao, C. Pei, B. Zhang, Z. Deng, M. Croft, Y. Qi, L. Yang, Y. Wang, X. Kuang, L. Jiang, D.-X. Yao, J.-G. Cheng and M.-R. Li, *CCS Chem.*, 2023, **5**, 934–946.

93 D. J. Rizzo, B. S. Jessen, Z. Sun, F. L. Ruta, J. Zhang, J. Q. Yan, L. Xian, A. S. McLeod, M. E. Berkowitz, K. Watanabe, T. Taniguchi, S. E. Nagler, D. G. Mandrus, A. Rubio, M. M. Fogler, A. J. Millis, J. C. Hone, C. R. Dean and D. N. Basov, *Nano Lett.*, 2020, **20**, 8438–8445.

94 B. Zhou, R. Jing, W. Zheng, X. Chen, J. Sun, Z. Zhou, H. Wang, L. Wehmeier, E. Song, B. Cheng, Y. Dong, M. Cothrine, D. Mandrus, G. L. Carr, X. Du, E. A. Henriksen, D. N. Basov and M. Liu, *ACS Photonics*, 2025, **12**, 3082–3090.

95 R. A. Vitalone, B. S. Jessen, R. Jing, D. J. Rizzo, S. Xu, V. Hsieh, M. Cothrine, D. G. Mandrus, L. Wehmeier, G. L. Carr, V. Bisogni, C. R. Dean, J. C. Hone, M. Liu, M. I. Weinstein, M. M. Fogler and D. N. Basov, *ACS Nano*, 2024, **18**, 29648–29657.

96 D. J. Rizzo, E. Seewald, F. Zhao, J. Cox, K. Xie, R. A. Vitalone, F. L. Ruta, D. G. Chica, Y. Shao, S. Shabani, E. J. Telford, M. C. Strasbourg, T. P. Darlington, S. Xu, S. Qiu, A. Devarakonda, T. Taniguchi, K. Watanabe, X. Zhu, P. J. Schuck, C. R. Dean, X. Roy, A. J. Millis, T. Cao, A. Rubio, A. N. Pasupathy and D. N. Basov, *Nat. Commun.*, 2025, **16**, 1853.

97 F. L. Ruta, B. S. Y. Kim, Z. Sun, D. J. Rizzo, A. S. McLeod, A. Rajendran, S. Liu, A. J. Millis, J. C. Hone and D. N. Basov, *Nat. Commun.*, 2022, **13**, 3719.

98 Y. Luo, D. Ding, A. M. Mier Valdivia, D. T. Larson, S. Liu, H. K. Ng, J. Wu, K. Watanabe, T. Taniguchi, E. Kaxiras, H. Park, P. Kim and W. L. Wilson, *Nat. Commun.*, 2025, **16**, 10158.

99 J. Shen, M. Chen, V. Korostelev, H. Kim, P. Fathi-Hafshejani, M. Mahjouri-Samani, K. Klyukin, G.-H. Lee and S. Dai, *Appl. Phys. Rev.*, 2024, **11**, 021409.

100 D. J. Rizzo, M. Riehs, H. Liu, D. Shin, T. Taniguchi, K. Watanabe, A. Rubio, A. Velian and D. N. Basov, *Nano Lett.*, 2025, **25**, 14043–14050.

101 A. J. Sternbach, S. H. Chae, S. Latini, A. A. Rikhter, Y. Shao, B. Li, D. Rhodes, B. Kim, P. J. Schuck, X. Xu, X.-Y. Zhu, R. D. Averitt, J. Hone, M. M. Fogler, A. Rubio and D. N. Basov, *Science*, 2021, **371**, 617–620.

102 A. J. Sternbach, S. Latini, S. Chae, H. Hübener, U. De Giovannini, Y. Shao, L. Xiong, Z. Sun, N. Shi, P. Kissin, G.-X. Ni, D. Rhodes, B. Kim, N. Yu, A. J. Millis, M. M. Fogler, P. J. Schuck, M. Lipson, X.-Y. Zhu, J. Hone, R. D. Averitt, A. Rubio and D. N. Basov, *Nat. Commun.*, 2020, **11**, 3567.

103 T. D. Ngo, M. S. Choi, M. Lee, F. Ali, Y. Hassan, N. Ali, S. Liu, C. Lee, J. Hone and W. J. Yoo, *Adv. Sci.*, 2022, **9**, 2202465.

104 T. D. Ngo, T. Huynh, I. Moon, T. Taniguchi, K. Watanabe, M. S. Choi and W. J. Yoo, *Nano Lett.*, 2023, **23**, 11345–11352.

105 J. Pack, Y. Guo, Z. Liu, B. S. Jessen, L. Holtzman, S. Liu, M. Cothrine, K. Watanabe, T. Taniguchi, D. G. Mandrus, K. Barmak, J. Hone and C. R. Dean, *Nat. Nanotechnol.*, 2024, **19**, 948–954.

106 A. Borah, A. Nipane, M. S. Choi, J. Hone and J. T. Teherani, *ACS Appl. Electron. Mater.*, 2024, **6**, 3894–3900.

107 Y. Guo, J. Li, X. Zhan, C. Wang, M. Li, B. Zhang, Z. Wang, Y. Liu, K. Yang, H. Wang, W. Li, P. Gu, Z. Luo, Y. Liu, P. Liu, B. Chen, K. Watanabe, T. Taniguchi, X.-Q. Chen, C. Qin, J. Chen, D. Sun, J. Zhang, R. Wang, J. Liu, Y. Ye, X. Li, Y. Hou, W. Zhou, H. Wang and Z. Han, *Nature*, 2024, **630**, 346–352.

108 Z. Hu, X. Liu, P. L. Hernández-Martínez, S. Zhang, P. Gu, W. Du, W. Xu, H. V. Demir, H. Liu and Q. Xiong, *InfoMat*, 2022, **4**, e12290.

109 Z. Liu, E. V. Boström, D. Sun, J. Pack, M. Cothrine, K. Watanabe, T. Taniguchi, D. G. Mandrus, A. Rubio and C. R. Dean, *arXiv*, 2025, preprint, arXiv:2508.01027, DOI: 10.48550/arXiv:2508.01027.

110 S. Kim, J. H. Yun, T. Taniguchi, K. Watanabe, J. Falson, J. S. Kim, K. H. Jin, G. Y. Cho and Y. Kim, *Nat. Commun.*, 2026, **17**, 1306.

111 Y. Yu, K. Zhang, H. Parks, M. Babar, S. Carr, I. M. Craig, M. Van Winkle, A. Lyssenko, T. Taniguchi, K. Watanabe, V. Viswanathan and D. K. Bediako, *Nat. Chem.*, 2022, **14**, 267–273.

112 H. Wang, D.-R. Chen, Y.-C. Lin, P.-H. Lin, J.-T. Chang, J. Muthu, M. Hofmann and Y.-P. Hsieh, *ACS Nano*, 2024, **18**, 19828–19835.

113 C.-H. Chiang, C.-C. Lin, Y.-C. Lin, C.-Y. Huang, C.-H. Lin, Y.-J. Chen, T.-R. Ko, H.-L. Wu, W.-Y. Tzeng, S.-Z. Ho, Y.-C. Chen, C.-H. Ho, C.-J. Yang, Z.-W. Cyue, C.-L. Dong, C.-W. Luo, C.-C. Chen and C.-W. Chen, *J. Am. Chem. Soc.*, 2024, **146**, 23278–23288.

114 B. T. Beshir, K. O. Obodo and G. A. Asres, *RSC Adv.*, 2022, **12**, 13749.

115 W. Li, C. Liu, C. Gu, J.-H. Choi, S. Wang and J. Jiang, *J. Am. Chem. Soc.*, 2023, **145**, 4774–4783.

116 H. Ma, Z. Wang, W. Zhao, H. Ren, H. Zhu, Y. Chi and W. Guo, *J. Phys. Chem. Lett.*, 2022, **13**, 8484–8494.

117 P. Jamdagni, A. Kumar, S. Srivastava, R. Pandey and K. Tankeshwar, *Int. J. Hydrogen Energy*, 2024, **66**, 268–277.

118 D. M. Kennes, M. Claassen, L. Xian, A. Georges, A. J. Millis, J. Hone, C. R. Dean, D. N. Basov, A. N. Pasupathy and A. Rubio, *Nat. Phys.*, 2021, **17**, 155–163.

119 Q. Yan, T. Li, X. Gao, S. Vaidya, S. Dikshit, Y. Luo, S. Strauf, R. Moukaouine, A. Pershin, A. Gali, Z. Fang, H. Stanfield, I. J. Vera-Marun, M. Newburger, S. Singh, T. Zhu, M. Brotons-Gisbert, K. D. Jöns, B. D. Gerardot, B. S. Y. Kim, J. R. Schaibley, K. L. Seyler, J. Balgley, J. Hone, K. C. Fong, L. Wang, G. Burkard, Y. Zeng, T. Heindel, S. Ateş, T. Vogl and I. Aharonovich, *arXiv*, 2025, preprint, arXiv:2512.14973, DOI: 10.48550/arXiv:2512.14973.

120 T. Huynh, H. Y. Lee and B. S. Y. Kim, *2D Mater.*, 2026, DOI: 10.1088/2053-1583/ae4ca3.

121 D. N. Basov, R. D. Averitt and D. Hsieh, *Nat. Mater.*, 2017, **16**, 1077–1088.

122 D. Jariwala, T. J. Marks and M. C. Hersam, *Nat. Mater.*, 2017, **16**, 170–181.

123 Y. Liu, Y. Huang and X. Duan, *Nature*, 2019, **567**, 323–333.

124 A. Castellanos-Gomez, X. Duan, Z. Fei, H. R. Gutierrez, Y. Huang, X. Huang, J. Quereda, Q. Qian, E. Sutter and P. Sutter, *Nat. Rev. Methods Primers*, 2022, **2**, 58.

125 F. Cui, V. García-López, Z. Wang, Z. Luo, D. He, X. Feng, R. Dong and X. Wang, *Chem. Rev.*, 2025, **125**, 445–520.

126 J. Park, A. N. Batyrkhanov, J. R. Schaibley and O. L. A. Monti, *Appl. Phys. Lett.*, 2024, **124**, 140502.

127 P. V. Pham, S. C. Bodepudi, K. Shehzad, Y. Liu, Y. Xu, B. Yu and X. Duan, *Chem. Rev.*, 2022, **122**, 6514–6613.

128 Y. Meng, J. Feng, S. Han, Z. Xu, W. Mao, T. Zhang, J. S. Kim, I. Roh, Y. Zhao, D.-H. Kim, Y. Yang, J.-W. Lee, L. Yang, C.-W. Qiu and S.-H. Bae, *Nat. Rev. Mater.*, 2023, **8**, 498–517.

129 R. Jacobs, J. Booske and D. Morgan, *Adv. Funct. Mater.*, 2016, **26**, 5471–5482.

130 D. Lu, D. J. Baek, S. S. Hong, L. F. Kourkoutis, Y. Hikita and H. Y. Hwang, *Nat. Mater.*, 2016, **15**, 1255–1260.

131 H. S. Kum, H. Lee, S. Kim, S. Lindemann, W. Kong, K. Qiao, P. Chen, J. Irwin, J. H. Lee, S. Xie, S. Subramanian, J. Shim, S.-H. Bae, C. Choi, L. Ranno, S. Seo, S. Lee, J. Bauer, H. Li, K. Lee, J. A. Robinson, C. A. Ross, D. G. Schlom, M. S. Rzchowski, C.-B. Eom and J. Kim, *Nature*, 2020, **578**, 75–81.

132 K. J. Rietwyk, D. A. Keller, A. Ginsburg, H.-N. Barad, M. Priel, K. Majhi, Z. Yan, S. Tirosh, A. Y. Anderson, L. Ley and A. Zaban, *Adv. Mater. Interfaces*, 2019, **6**, 1802058.

133 K. P. Harikrishnan, X. Wei, C.-H. Lee, D. Yoon, Y. Lee, K. J. Crust, Y.-T. Shao, R. Xu, J. H. Kang, C. Liang, J. Park, H. Y. Hwang and D. A. Muller, *Adv. Mater.*, 2026, e21189.

134 K. Lee, T. D. Ngo, S. Lee, H. Shin, M. S. Choi, J. Hone and W. J. Yoo, *Adv. Electron. Mater.*, 2023, **9**, 2200955.

135 Y. Guo, J. Li, X. Zhan, C. Wang, M. Li, B. Zhang, Z. Wang, Y. Liu, K. Yang, H. Wang, W. Li, P. Gu, Z. Luo, Y. Liu, P. Liu, B. Chen, K. Watanabe, T. Taniguchi, X.-Q. Chen, C. Qin, J. Chen, D. Sun, J. Zhang, R. Wang, J. Liu, Y. Ye, X. Li, Y. Hou, W. Zhou, H. Wang and Z. Han, *Nature*, 2024, **630**, 346–352.

136 Y.-C. Lin, B. M. Bersch, R. Addou, K. Xu, Q. Wang, C. M. Smyth, B. Jariwala, R. C. Walker II, S. K. Fullerton-Shirey, M. J. Kim, R. M. Wallace and J. A. Robinson, *Adv. Mater. Interfaces*, 2020, **7**, 2000422.

137 F. Boschini, M. Zonno and A. Damascelli, *Rev. Mod. Phys.*, 2024, **96**, 015003.

138 M. Reutzel, G. S. M. Jansen and S. Mathias, *Adv. Phys. X*, 2024, **9**, 1–44.

139 R. Hillenbrand, Y. Abate, M. Liu, X. Chen and D. N. Basov, *Nat. Rev. Mater.*, 2025, **10**, 285–310.

140 M. A. Huber, F. Mooshammer, M. Plankl, L. Viti, F. Sandner, L. Z. Kastner, T. Frank, J. Fabian, M. S. Vitiello, T. L. Cocker and R. Huber, *Nat. Nanotechnol.*, 2017, **12**, 207–211.

141 M. Plankl, P. E. Faria Junior, F. Mooshammer, T. Siday, M. Zizlsperger, F. Sandner, F. Schiegl, S. Maier, M. A. Huber, M. Gmitra, J. Fabian, J. L. Boland, T. L. Cocker and R. Huber, *Nat. Photonics*, 2021, **15**, 594–600.

142 T. L. Cocker, V. Jelic, M. Gupta, S. J. Molesky, J. A. J. Burgess, G. De Los Reyes, L. V. Titova, Y. Y. Tsui, M. R. Freeman and F. A. Hegmann, *Nat. Photonics*, 2013, **7**, 620–625.

143 K. Yoshioka, I. Katayama, Y. Minami, M. Kitajima, S. Yoshida, H. Shigekawa and J. Takeda, *Nat. Photonics*, 2016, **10**, 762–765.

144 T. L. Cocker, D. Peller, P. Yu, J. Repp and R. Huber, *Nature*, 2016, **539**, 263–267.

145 V. Jelic, K. Iwaszczuk, P. H. Nguyen, C. Rathje, G. J. Hornig, H. M. Sharum, J. R. Hoffman, M. R. Freeman and F. A. Hegmann, *Nat. Phys.*, 2017, **13**, 591–598.

146 G. Gramse, A. Kölker, T. Lim, T. J. Z. Stock, H. Solanki, S. R. Schofield, E. Brinciotti, G. Aeppli, F. Kienberger and N. J. Curson, *Sci. Adv.*, 2017, **3**, e1602586.

147 M. E. Barber, E. Y. Ma and Z.-X. Shen, *Nat. Rev. Phys.*, 2022, **4**, 61–74.

148 L. W. Cao, C. Wu, L. Lyu, L. Cohen, N. Samuelson, Z. Yan, S. Pancholi, K. Watanabe, T. Taniguchi, D. E. Parker, A. F. Young and M. T. Allen, *arXiv*, 2025, preprint, arXiv:2508.18365, DOI: 10.48550/arXiv:2508.18365.

149 F. Krausz and M. Ivanov, *Rev. Mod. Phys.*, 2009, **81**, 163–234.

150 K. Choudhary, I. Kalish, R. Beams and F. Tavazza, *Sci. Rep.*, 2017, **7**, 5179.

151 K. T. Butler, D. W. Davies, H. Cartwright, O. Isayev and A. Walsh, *Nature*, 2018, **559**, 547–555.

152 J. Schmidt, M. R. G. Marques, S. Botti and M. A. L. Marques, *npj Comput. Mater.*, 2019, **5**, 83.

153 K. Choudhary, B. DeCost, C. Chen, A. Jain, F. Tavazza, R. Cohn, C. W. Park, A. Choudhary, A. Agrawal, S. J. L. Billinge, E. Holm, S. P. Ong and C. Wolverton, *npj Comput. Mater.*, 2022, **8**, 59.

154 D. Willhelm, N. Wilson, R. Arroyave, X. Qian, T. Cagin, R. Pachter and X. Qian, *ACS Appl. Mater. Interfaces*, 2022, **14**, 25907–25919.

155 L. Shen, J. Zhou, T. Yang, M. Yang and Y. P. Feng, *Acc. Mater. Res.*, 2022, **3**, 572–583.

156 P. Lyngby and K. S. Thygesen, *npj Comput. Mater.*, 2022, **8**, 232.

157 K. Choudhary, K. F. Garrity, S. T. Hartman, G. Pilania and F. Tavazza, *Phys. Rev. Mater.*, 2023, **7**, 014009.

158 E. Gerber, S. B. Torrisi, S. Shabani, E. Seewald, J. Pack, J. E. Hoffman, C. R. Dean, A. N. Pasupathy and E.-A. Kim, *Nat. Commun.*, 2023, **14**, 7921.

159 A. Kanwal, A. Jalil and S. R. A. Raza, *J. Phys. Chem. C*, 2025, **129**, 205–218.

160 S. Gao, Q. Huang, C. Huang, C. Li, K. Liu, B. Sa, Y. Yu, D. Xue, Z. Liu and M. Dai, *Sci. Rep.*, 2025, **15**, 23023.

161 X. Liu, Y. Li, X. Zhang, Y.-M. Zhao, X. Wang, J. Zhou, J. Shen, M. Zhou and L. Shen, *J. Mater. Chem. A*, 2025, **13**, 5649–5660.

162 F. Shobeyrian, M. Soleimani, F. Shojaei, A. L. Zand and M. Pourfath, *ACS Appl. Energy Mater.*, 2025, **8**, 9748–9759.

163 L. Hörmann, W. G. Stark and R. J. Maurer, *npj Comput. Mater.*, 2025, **11**, 196.

164 A. L. Araújo, P. H. Sophia, F. C. de Lima and A. Fazzio, *npj Comput. Mater.*, 2025, **11**, 42.

165 R. Arora, A. R. Barr, D. T. Larson, M. Pizzochero and E. Kaxiras, *Phys. Rev. Mater.*, 2025, **9**, L021601.

166 C. A. Vital, R. J. Armenta-Rico and H. E. Sauceda, *arXiv*, 2025, preprint, arXiv:2503.05845, DOI: 10.48550/arXiv:2503.05845.

167 N. J. Szymanski, B. Rendy, Y. Fei, R. E. Kumar, T. He, D. Milsted, M. J. McDermott, M. Gallant, E. D. Cubuk, A. Merchant, H. Kim, A. Jain, C. J. Bartel, K. Persson, Y. Zeng and G. Ceder, *Nature*, 2023, **624**, 86–91.

168 S. Masubuchi, M. Morimoto, S. Morikawa, M. Onodera, Y. Asakawa, K. Watanabe, T. Taniguchi and T. Machida, *Nat. Commun.*, 2018, **9**, 1413.

169 B. Han, Y. Lin, Y. Yang, N. Mao, W. Li, H. Wang, K. Yasuda, X. Wang, V. Fatemi, L. Zhou, J. I.-J. Wang, Q. Ma, Y. Cao, D. Rodan-Legrain, Y.-Q. Bie, E. Navarro-Moratalla, D. Klein, D. MacNeill, S. Wu, H. Kitadai, X. Ling, P. Jarillo-Herrero, J. Kong, J. Yin and T. Palacios, *Adv. Mater.*, 2020, **32**, 2000953.

170 E. D. S. Courtney, M. Pendharkar, N. J. Bittner, A. L. Sharpe and D. Goldhaber-Gordon, *Rev. Sci. Instrum.*, 2025, **96**, 053907.

171 J.-L. Uslu, A. Nekrasov, A. Hermans, B. Beschoten, B. Leibe, L. Waldecker and C. Stampfer, *Digital Discovery*, 2025, **4**, 3744–3755.

172 F. Yang, W. Idehara, K. Tanaka, K. Shinokita, H. Zhao and K. Matsuda, *ACS Nano*, 2025, **19**, 39005–39015.

173 P. A. Leger, A. Ramesh, T. Ulloa and Y. Wu, *Sci. Rep.*, 2024, **14**, 27808.